

Eastward-Propagating Planetary Waves Prior to Sudden Stratospheric Warmings

Christian Todd Rhodes¹, Varavut Limpasuvan¹, and Yvan Orsolini²

¹Coastal Carolina University

²Norwegian Institute for Air Research

November 24, 2022

Abstract

The sources and characteristics of the slow eastward-propagating planetary waves (EPWs) were investigated prior to the major sudden stratospheric warming (SSW) events, as observed by the Microwave Limb Sounder (MLS) and simulated by the National Center for Atmospheric Research (NCAR) Whole Atmosphere Community Climate Model (WACCM) with specified dynamics. With a zonal phase speed of $\sim 10 \text{ m s}^{-1}$, these EPWs appeared as wavenumber-1 and -2 perturbations in the boreal stratosphere and mesosphere prior to SSWs with split and displaced polar vortex. Found near the turning and critical layers, these waves were manifestations of an unstable eastward mesospheric flow. These instability waves were investigated from the perspective of over-reflection. A zonal-mean zonal wind structure with local maxima around the upper polar stratosphere and the subtropical mesosphere was commonly found prior to SSW onset as the result of net forcing by gravity and planetary waves. This structure was largely unstable and provided the wave geometry conducive to over-reflection.

1 **Eastward-Propagating Planetary Waves Prior to Sudden Stratospheric Warmings**

2 **Christian Rhodes¹, Varavut Limpasuvan¹, Yvan Orsolini²**

3 ¹School of Coastal and Marine Systems Science, Coastal Carolina University, Conway, South
4 Carolina, USA, ²Norwegian Institute for Air Research (NILU), Kjeller, Norway.

5 Corresponding author: Christian Rhodes (ctrhodes@coastal.edu)

6 **Key Points:**

- 7 • Before major sudden stratospheric warmings, planetary and gravity waves form a middle
8 atmosphere double-maxima zonal wind structure.
- 9 • The double-maxima wind configuration favors instability planetary wave growth via
10 over-reflection.
- 11 • The refractive index of the wintertime middle atmosphere reveals an inherent bias to
12 produce instability waves with eastward phase speeds.

13 Abstract

14 The sources and characteristics of the slow eastward-propagating planetary waves (EPWs) were
15 investigated prior to the major sudden stratospheric warming (SSW) events, as observed by the
16 Microwave Limb Sounder (MLS) and simulated by the National Center for Atmospheric
17 Research (NCAR) Whole Atmosphere Community Climate Model (WACCM) with specified
18 dynamics. With a zonal phase speed of $\sim 10 \text{ m}\cdot\text{s}^{-1}$, these EPWs appeared as wavenumber-1 and -2
19 perturbations in the boreal stratosphere and mesosphere prior to SSWs with split and displaced
20 polar vortex. Found near the turning and critical layers, these waves were manifestations of an
21 unstable eastward mesospheric flow. These instability waves were investigated from the
22 perspective of over-reflection. A zonal-mean zonal wind structure with local maxima around the
23 upper polar stratosphere and the subtropical mesosphere was commonly found prior to SSW
24 onset as the result of net forcing by gravity and planetary waves. This structure was largely
25 unstable and provided the wave geometry conducive to over-reflection.

26 1 Introduction

27 The wintertime structure of the stratosphere and mesosphere arises from the competing
28 effects between net radiative heating and wave forcing (Andrews et al., 1987). The main source
29 of stratospheric variability is upward-propagating planetary waves (PWs) generated in the
30 troposphere by large-scale orography and heat sources (e.g., Charney & Eliassen, 1949;
31 Smagorinsky, 1953). During the Northern Hemisphere (NH) winter, the prevailing eastward flow
32 of the polar night jet allows PWs to propagate into the stratosphere and, upon their dissipation,
33 impact the flow. Above the stratosphere, gravity waves (GWs) from tropospheric sources (e.g.,
34 convection, fronts, and small-scale orography) play an important role. In particular, the breaking
35 of upward-propagating GWs with westward phase speeds imposes a strong westward drag on the
36 eastward flow, capping the top of the polar night jet and modulating the polar stratopause (Duck
37 et al., 2001; Leovy, 1964). However, variations in strength and direction of the lower
38 stratospheric winds can usher GWs of different zonal phase speeds into the mesosphere,
39 affecting the gravity wave drag (GWD) distribution near the top of the polar night jet. Overall,
40 the combined influence of GWs and PWs keeps the polar vortex warmer than otherwise under
41 radiative equilibrium.

42 Occasionally, when the upward PW activity is large, its eventual dissipation in the NH
43 winter polar stratosphere can strongly decelerate the zonal-mean zonal wind (\bar{u}). Subsequently, \bar{u}
44 can reverse direction as the polar region undergoes rapid warming (Matsuno, 1971), resulting in
45 a phenomenon called a major sudden stratospheric warming (SSW). Occurring roughly 60% of
46 NH winters (e.g., Butler et al., 2015), SSWs are also characterized by the highly perturbed
47 stratospheric polar vortex becoming split (i.e., split SSW) or highly displaced off the North Pole
48 (i.e., displaced SSW). The impacts of SSWs have been linked to anomalously cold conditions
49 over Europe and Northeast America (e.g., Baldwin & Dunkerton, 2001) and atypical atmospheric
50 perturbations above the stratosphere (Goncharenko et al., 2010; Limpasuvan et al., 2016;
51 Pedatella et al., 2016; Sassi et al., 2016).

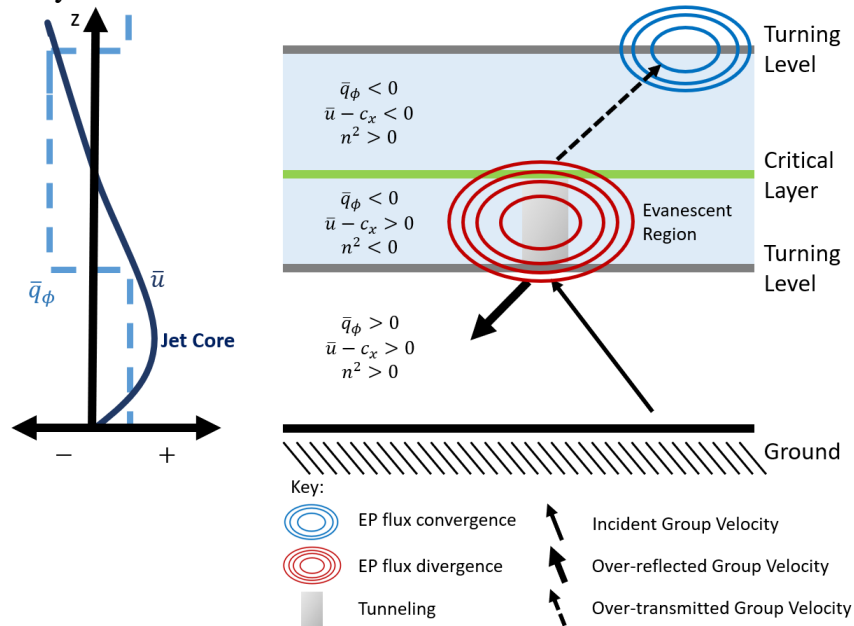
52 The zonal-mean zonal wind structure in the stratosphere and mesosphere can exhibit
53 regions of unusually strong wind shear. There, the flow can become barotropically or
54 baroclinically unstable, leading to the appearance of unstable PWs (e.g., Dickinson, 1973; C. B.
55 Leovy & Webster, 1976; Matthias & Ern, 2018). For shear instability to occur, the generally
56 positive meridional (quasi-geostrophic) potential vorticity gradient (\bar{q}_ϕ) associated with the

57 wintertime circulation must become negative (e.g., Salby, 1996). To serve as a source for an
58 instability wave of a certain zonal phase speed (c_x), that region must also contain a critical layer,
59 where the mean zonal flow matches c_x (Dickinson, 1973). Hartmann (1983) used a linear
60 barotropic model and a quasi-geostrophic baroclinic model to examine instabilities of the
61 eastward stratospheric polar night jet. He found that, when the instability was seated on the
62 poleward flank of the jet, the most unstable modes were wavenumber-1 and -2 waves with
63 periods of a few days. When the instability was seated on the mid-latitude flank of the jet, the
64 most unstable modes were wavenumber-1 to -3 waves with periods of a week or more. Manney
65 et al. (1988) suggests that these periods are likely slightly longer in observations since the
66 nonlinear effect of instability tends to weaken and broaden the jet (Pedlosky, 1987). Orsolini &
67 Simon (1995) used a fully nonlinear nondivergent barotropic model to simulate the generation
68 and life cycle of unstable PWs arising from the instability of the polar night jet, as well those
69 arising from the instability of a double jet representing the mesospheric subtropical jet and the
70 upward extension of the stratospheric polar night jet. These authors found similar low-
71 wavenumber instability waves as Hartmann (1983) with periods on the order of days for the
72 single jet case. Planetary-scale vortices developed to expel the low potential vorticity on the
73 poleward flank of the jet into lower latitudes, acting to remove the sign reversal of the meridional
74 potential vorticity gradient. Eddies of higher wavenumbers (3-4) were found in the double-jet
75 case, accelerating and stabilizing the flow between the two zonal wind maxima. Although
76 perturbations of higher wavenumbers have larger growth rates, Hartmann (1983) suggested that
77 low-wavenumber instabilities (given the predominance of low-wavenumber disturbance in the
78 stratosphere) would be more likely to derive energy from an unstable flow than higher
79 wavenumbers.

80 Prior to the split SSW of January 2009, a couple of studies noted the presence of slow
81 eastward-propagating PWs, hereafter EPWs, in the mesosphere (L. Coy et al., 2011; Iida et al.,
82 2014). Using a high-top forecast model with data assimilation, Coy et al. (2011) suggested that
83 the mesospheric EPWs directly propagated from the troposphere with the underlying bursts of
84 wavenumber-2 PW activity prior to the SSW onset and their eventual dissipation in the lower
85 mesosphere. Using satellite observations, Iida et al. (2014) noted that the EPW appearance
86 before SSW onset could be generated by *in situ* shear instability of the polar night jet. Regardless
87 of their source, EPWs may be a common feature leading up to SSW. In the composite study of
88 Limpasuvan et al. (2016) based on 13 SSW events, a robust signature of zonal wavenumber-1
89 EPW with an eastward period of around 10 days was clearly evident between 40-60 km and over
90 the polar region, intensifying roughly 10 days before SSW onset (see their Figure 10). However,
91 these authors did not discuss the cause of the wave presence and focused only on the
92 wavenumber-1 westward-travelling wave, developing after the SSW onset. Hence, the exact
93 nature of EPWs and why they occur before SSW onset remain unclear.

94 In general, propagating PWs can interact with a pre-existing unstable region (where \bar{q}_ϕ is
95 negative) and over-reflect (Harnik & Heifetz, 2007). Following Lindzen et al. (1980), **Figure 1**
96 illustrates this scenario for a simplified atmosphere with some assumed \bar{u} vertical profile. Over-
97 reflection occurs when an incident PW reflects from the unstable region with more energy than it
98 initially had (thick arrow). At the turning level (indicated by the \bar{q}_ϕ sign change), the incident
99 PW can tunnel through the evanescent region (where the wave amplitude diminishes
100 exponentially with height) before eventually reaching the critical layer (where the squared
101 refractive index n^2 also changes sign). An associated over-transmission occurs when diminished

102 PW emerges from the critical layer with more energy than the incident PW. In this circumstance,
 103 an instability wave can manifest an over-reflected component emanating downward from the
 104 turning level and an over-transmitted component emerging from the critical layer (Dickinson,
 105 1973). If the evanescent region is sufficiently thin, the exponentially decaying waves can readily
 106 reach the critical layer.



107
 108

109 **Figure 1.** A schematic of PW over-reflection with background \bar{u} and \bar{q}_ϕ fields shown on
 110 the left with arbitrary magnitudes. On the right, upward-propagating PWs (thin solid arrow)
 111 over-reflect at the turning level, resulting in a reflected wave (thick solid arrow) with enhanced
 112 energy. A transmitted wave (thin dashed arrow) appears above the critical layer. The light blue
 113 shading indicates the negative \bar{q}_ϕ region.

114 Through this over-reflection perspective, instability waves are manifestations of
 115 stimulated emissions from the unstable flow region. As such, the upward EPWs burst noted by
 116 Coy et al. (2011) and the instability EPWs observed by Iida et al. (2014) prior to SSW may not
 117 be independent in the context of Figure 1.

118 The present study evaluates the source and characteristics of mesospheric EPWs prior to
 119 SSWs using a high-top general circulation model and global satellite observations. Based on
 120 several SSW events and their composite, we attempt to examine the roles of GWs and PWs in
 121 fostering changes in the background mesospheric wind leading up to SSW onset and the EPW
 122 presence. Focus is placed on the interplay of wave geometry and the roles of over-reflection and
 123 over-transmission with respect to shear instability that manifests as EPWs. To our knowledge,
 124 this is the first study to examine the mesospheric instabilities prior to SSW events from such
 125 perspective. From the basis of mesosphere-stratosphere coupling prior to SSW, our results may
 126 help assess the role of the mesosphere in SSW predictability. Our findings reveal the appearance
 127 of robust and unique double-maxima wind structure set up by GWs and PWs prior to SSW. This
 128 wind structure is conducive for the occurrence of strong and persistent EPWs. Appearing in the
 129 mesosphere as wavenumber-1 and wavenumber-2 perturbations before both split and displaced

130 SSWs, EPWs are manifestations of shear instability as well as over-reflection by upward-
131 propagating PWs.

132 2. Methods

133 2.1 Model and Observations

134 We utilized the Whole Atmosphere Community Climate Model, Version 4 (WACCM)
135 developed at the National Center for Atmospheric Research (NCAR). As part of the Community
136 Earth System Model Version 1.2, WACCM is an atmosphere-only global chemistry-climate
137 model that extends up to ~ 145 km (5.1×10^{-6} hPa). Details of WACCM are provided by Marsh et
138 al. (2013). Notable model features include parameterization of GWD generated by convection
139 and fronts as well as mountain stresses which have improved the frequency of SSWs in the
140 Northern Hemisphere (Richter et al., 2010).

141 WACCM was run in the specified dynamics configuration from 1980 to 2013. Referred
142 to as WACCM-SD, this configuration has a horizontal resolution of 0.95° latitude by 1.25°
143 longitude, 88 vertical levels, and key dynamical variables output daily. The model's temperature
144 and dynamics are constrained up to 50 km with six-hourly Modern-Era Retrospective Analysis
145 for Research and Application (MERRA) Version 2 reanalysis (Gelaro et al., 2017). A linear
146 transition is applied between the nudged output below 50 km and the overlying (fully interactive)
147 free-running region above 60 km.

148 Model results were compared to observations from the Microwave Limb Sounder (MLS)
149 aboard the polar-orbiting NASA Earth Observing System Aura satellite. Geopotential height are
150 retrieved from the 118-GHz (2.54 mm wavelength) and 234-GHz (1.28 mm wavelength) O₂
151 spectral lines and temperature from the 118-GHz and 239-GHz (1.23 mm wavelength) O₂
152 spectral lines. Both variables are useful between 261 hPa and 0.001 hPa (Livesey et al., 2017).
153 Orbiting the Earth ~ 15 times per day, the satellite provides near-daily global coverage when
154 combining measurements from both the ascending and descending tracks.

155 2.2 SSW Identification and Classification

156 SSW identification has been traditionally based on the World Meteorological
157 Organization (WMO) definition, dating back to 1952 when the first SSW was initially observed
158 (Scherhag, 1952). Over the years, variation of this definition has crept into practice (Butler et al.,
159 2015). Studies focused on the coupling between SSW and the mesosphere-lower thermosphere
160 (MLT) region may specialize to SSW events during which the vortex recovery is accompanied
161 by a stratopause elevated above its climatological altitude (Manney et al., 2008). These
162 specialized SSWs with an elevated stratopause are referred to as ES-SSWs. Based on the zonal-
163 mean zonal wind and temperature averaged between 70°N and 90°N during the extended winter,
164 Limpasuvan et al. (2016) identified an ES-SSW event if: (1) the temperature falls below 190 K
165 between 80-100 km, (2) the zonal-mean zonal wind reverses from eastward to westward at 1 hPa
166 and persists longer than 5 days, and (3) the stratopause altitude based on the zonal-mean
167 temperature maximum between 20-100 km exhibits a vertical discontinuity of at least 10 km.
168 With focus on the upper-stratospheric and mesospheric dynamics pertinent in this study, these
169 criteria are used here to identify SSW onset dates and listed in **Table 1**. Between 1984 and 2013,
170 13 SSW events are identified. To consider the diversity of EPW occurrences, we note in Table 1
171 how the SSWs were classified (as either split or displaced) based on past studies. We emphasize
172 that the onset is defined based on a zonal-mean zonal wind reversal at 1 hPa.

Onset year (YYYY)	Onset date (MM-DD)	Classification by other studies
1984	02-21	Displaced (Charlton & Polvani, 2007)
1984	12-30	Split (Charlton & Polvani, 2007)
1987	01-22	Displaced (Charlton & Polvani, 2007)
1989	02-19	Split (Charlton & Polvani, 2007)
1995	01-27	Not Present
1997	12-23	Not Present
2002	02-13	Displaced (Charlton & Polvani, 2007)
2003	12-20	Displaced (Kuttippurath & Nikulin, 2012)
2006	01-09	Displaced (Kuttippurath & Nikulin, 2012)
2009	01-22	Split (Manney et al. 2009, Kuttippurath & Nikulin, 2012)
2010	01-24	Displaced (Kuttippurath & Nikulin, 2012)
2012	01-13	Displaced (Chandran et al., 2013)
2013	01-05	Split (Coy & Pawson, 2015)

173 **Table 1.** Identification and classification of SSWs from 1979 to 2013. SSW onset dates
174 were defined by the point of wind reversal at 1 hPa. Each event identified qualifies as an ES-
175 SSW according to criteria from Limpasuvan et al. (2016). The SSW type was classified by
176 multiple studies (Chandran et al., 2013; Charlton & Polvani, 2007; Lawrence Coy & Pawson,
177 2015; Kuttippurath & Nikulin, 2012; Manney et al., 2009).

178

179 2.3 Data Analyses

180 EPWs were identified by bandpass filtering specific wavenumbers over a range of
181 eastward phase speeds. Using Fourier transform, a Hanning window spanning 31 days was
182 applied such that subseasonal variations were captured. To alleviate the dampening effect of the
183 Hanning window, the Fourier transform was performed daily such that the window straddled a
184 central date (a sliding window). The Eliassen-Palm (EP) flux was calculated following the
185 formulation in Andrews et al. (1987) and based on 5-day averages of dependent field variables
186 (wind, temperature, etc.). While this inherently filtered out waves with periods < 5 days (or with
187 $c_x > 46 \text{ m}\cdot\text{s}^{-1}$ at 60°N), this was well below the expected period of > 14 days (or $c_x < 20 \text{ m}\cdot\text{s}^{-1}$ at
188 $30\text{-}50^\circ\text{N}$) suggested by Coy et al. (2011). For MLS, the vertical velocity and vertical fluxes were
189 neglected in the EP flux calculation. Regardless, these components were negligible in the EP flux
190 calculation of the model data.

191 For MLS, the horizontal winds were calculated from the observed geopotential based on
 192 the geostrophic wind approximation shown in Iida et al. (2014). A running 3-day average was
 193 applied to appropriate variables before computing \bar{q}_ϕ (O'Neill & Youngblut, 1982):

$$\bar{q}_\phi = 2\Omega \cos\phi - R_e^{-1} \frac{\partial}{\partial\phi} \left(\frac{1}{\cos\phi} \frac{\partial(\bar{u} \cos\phi)}{\partial\phi} \right) - \frac{R_e f^2}{\bar{\rho}} \frac{\partial}{\partial z} \left(\frac{\bar{\rho}}{N_B^2} \frac{\partial\bar{u}}{\partial z} \right) \quad (1)$$

194 where ϕ is the latitude, z the log-pressure height, f the Coriolis parameter, N_B the Brunt-Väisälä
 195 frequency, $\bar{\rho}$ the zonal-mean atmospheric density, Ω the Earth's angular frequency, and R_e the
 196 Earth's radius. In later discussion, we refer to the positive definite first term on the right hand
 197 side (RHS) as the “beta term” associated with the gradient of f , the second term as the
 198 “barotropic term” associated with horizontal wind curvature, and the third term as the “baroclinic
 199 term” associated mainly with the vertical wind curvature. The squared refractive index (n^2) can
 200 be used to better understand how PWs of certain zonal wavenumbers (s) and zonal phase speeds
 201 (c_x) propagate in \bar{u} (Andrews et al., 1987):

$$n^2 = \frac{\bar{q}_\phi}{R_e(\bar{u} - c_x)} - \left(\frac{s}{R_e \cos\phi} \right)^2 - \left(\frac{f}{2N_B H} \right)^2 \quad (2)$$

202 where H is the scale height. PWs tend to propagate towards a large positive squared refractive
 203 index and are unable to propagate in regions with a negative squared refractive index. In figures,
 204 \bar{q}_ϕ and n^2 are nondimensionalized by Ω and R_e^2 , respectively.

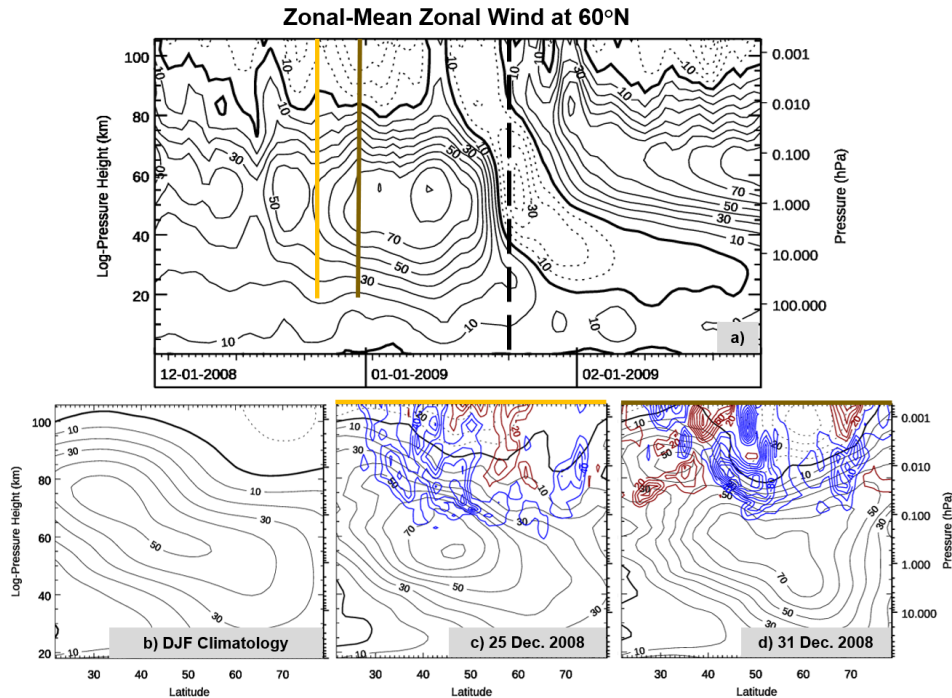
205 Following Coy et al. (2011), the presence of a wave with a specific wavenumber was
 206 detected if the geopotential height perturbation (GHP) amplitude exceeded 200 m. After binning
 207 the geopotential height amplitude by phase speed, the mean phase speed and standard deviation
 208 were calculated. A critical layer was identified if the background wind was within 0.05 standard
 209 deviations of the mean phase speed and the GHP amplitude exceeded 200 m.

210 3 January 2009 Split SSW Case

211 The mesospheric PWs prior to the January 2009 split SSW event are first investigated. A
 212 focus on this particular case allows the present study's findings to be substantiated by those of
 213 Coy et al. (2011) and Iida et al. (2014). This split SSW event was associated with very strong
 214 polar warming of more than 50 K in a matter of days (e.g., Harada et al., 2010).

215 In WACCM-SD, SSW onset occurs on 22 January 2009 (see Table 1). Evident in **Figure**
 216 **2a**, the upper-mesospheric zonal-mean zonal winds reversed ~5 days prior to the onset date
 217 indicated by the vertical dashed line. The early reversal of the upper-mesospheric wind before
 218 SSW onset is also evident in the MLS observations of Iida et al. (2014). In the stratosphere and
 219 lower mesosphere, the polar jet strengthened a few days prior to wind reversal. Gold and brown
 220 vertical bars in Figure 2a mark selected time slices of the meridional cross-sections of the zonal-
 221 mean zonal wind shown in Figures 2c and 2d. The zonal-mean zonal wind climatology (devoid
 222 of ES-SSWs listed in Table 1) in Figure 2b is shown for comparison. By 31 December, the
 223 eastward winds had strengthened compared to climatology. Furthermore, a double-maxima wind
 224 configuration had developed with a distinct eastward mid-latitude core near the stratopause and
 225 an eastward low-latitude subtropical core near 80 km, both with speed exceeding $60 \text{ m}\cdot\text{s}^{-1}$.

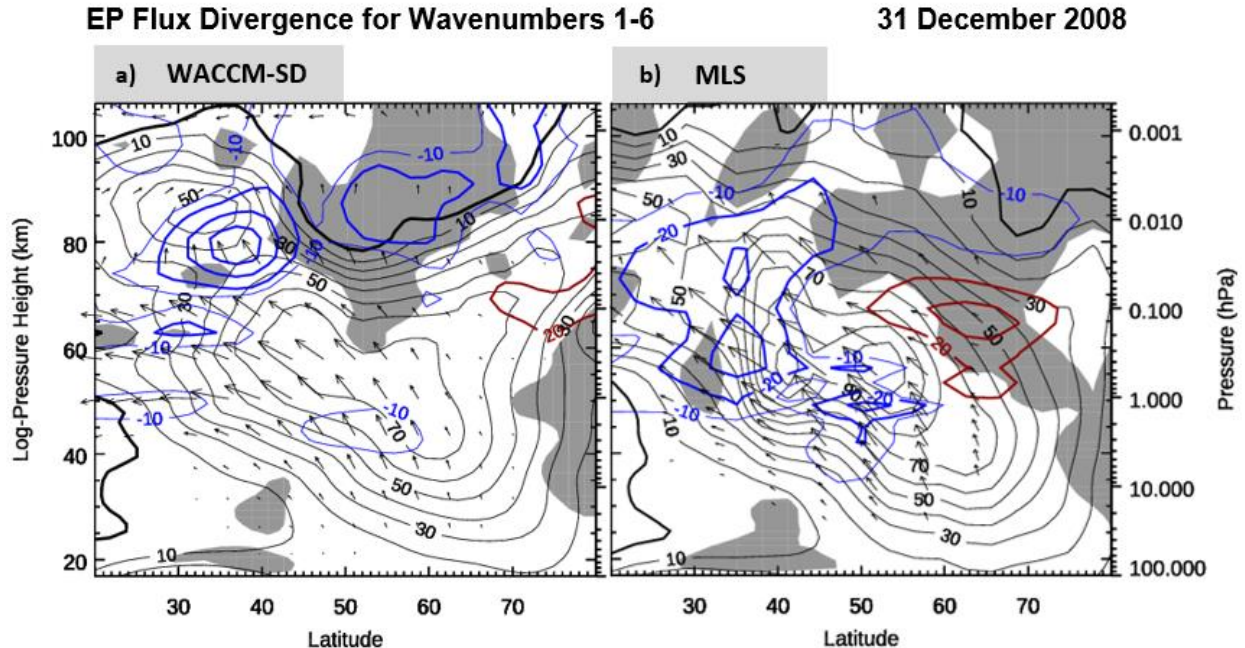
226 Throughout December, GW dissipation capped the eastward jet in the mid- to high-latitudes with
 227 local westward drag (blue contours) of more than $80 \text{ m}\cdot\text{s}^{-1}\cdot\text{day}^{-1}$, maintaining the zero-wind line
 228 above 80 km.



229 **Figure 2.** (a) Polar-averaged zonal-mean zonal wind (\bar{u}) evolution during the 2009 split
 230 SSW event with an onset date of 22 January as indicated by a vertical dashed line. (b) The
 231 December-February \bar{u} climatology for the 1980-2013 period without ES-SSWs. (c) and (d) \bar{u} for
 232 25 and 31 December 2008, respectively. For all, the westward (dotted black contour) and
 233 eastward (solid thin black contour) wind is contoured every $10 \text{ m}\cdot\text{s}^{-1}$, with the zero-wind line
 234 thickened. Incremented by $20 \text{ m}\cdot\text{s}^{-1}\cdot\text{day}^{-1}$, GW drag (resolved and parameterized in the model) is
 235 contoured in blue for westward forcing and red for eastward forcing.
 236

237 3.1 Formation of a Double-Maxima Wind Structure

238 The formation of a double-maxima wind configuration between 25 and 31 December was
 239 investigated by examining the PW and GW forcings on the background wind. **Figure 3**
 240 illustrates PW forcing (for wavenumbers 1-6) during 31 December for both model and
 241 observations. The mesospheric zero-wind line is notably lower in the model than in observations,
 242 revealing a zonal wind bias in WACCM-SD up to $7 \text{ m}\cdot\text{s}^{-1}$ above 0.1 hPa (Rüfenacht et al., 2018).
 243 Centered near 35°N and 80 km, the EP flux convergence of PWs indicates strong wind
 244 deceleration (blue contours) in excess of $60 \text{ m}\cdot\text{s}^{-1}\cdot\text{day}^{-1}$ in WACCM-SD. The observations reveal
 245 a similar PW forcing, albeit weaker and at a slightly lower altitude. In either case, the
 246 decelerative wave forcing occurs between the subtropical and polar jet cores. Following the EP
 247 flux vectors, this flux convergence region mainly results from the dampening of PWs
 248 propagating from the troposphere.



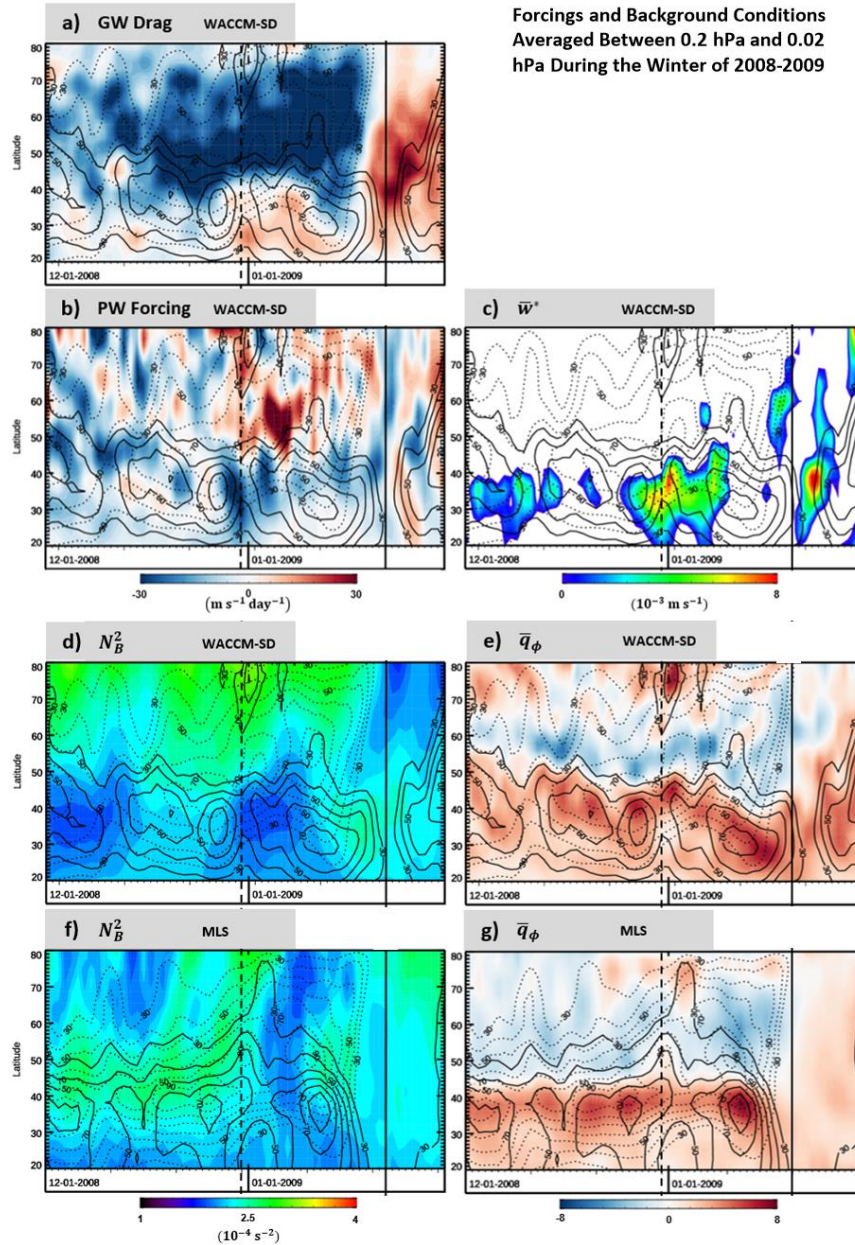
249
 250 **Figure 3.** Altitude vs. latitude sections of PW EP flux for (a) WACCM-SD and (b) MLS
 251 data during 31 December 2008. Negative and positive EP flux divergence values are contoured
 252 every $20 \text{ m}\cdot\text{s}^{-1}\cdot\text{day}^{-1}$ in thick blue and red lines, respectively. Indicating the $10 \text{ m}\cdot\text{s}^{-1}\cdot\text{day}^{-1}$
 253 isopleth, the thin blue contour illustrates the broad extent of PW forcing. The meridional EP Flux
 254 vector component was scaled by $(100\pi R_e \rho)^{-1} \cos \phi$ and the vertical component by
 255 $(R_e \rho)^{-1} \cos \phi$. The westward (dotted black contour) and eastward (solid thin black contour) \bar{u} is
 256 contoured every $10 \text{ m}\cdot\text{s}^{-1}$, with the zero-wind line thickened. The grey-shaded regions represent
 257 areas of negative \bar{q}_ϕ .

258 Wintertime PWs propagating upward from the troposphere can break along the edge of
 259 the polar vortex, as suggested by the EP flux pattern of Figure 3. The breaking process
 260 decelerates the equatorward flank of the polar night jet below 70 km. Subsequently, this
 261 weakened eastward wind allows eastward GWs to reach the mesosphere and impose an eastward
 262 GWD near the subtropical mesospheric jet core, shown in Figure 2d. Additionally, the presence
 263 of PW perturbations would introduce longitudinal variability in stratospheric wind field,
 264 allowing for the asymmetric upward GW transmittance.

265 While other studies have developed algorithms to estimate GWD with satellite data (Ern
 266 et al., 2004), we rely only on WACCM-SD to illuminate GW forcing. The total zonal GWD is
 267 determined by summing the parameterized and resolved GWD; the resolved GWD was estimated
 268 as the zonal EP flux divergence for waves of zonal wavenumbers greater than 6 (e.g., Fetzer &
 269 Gille, 1994). Nevertheless, we may indirectly assess GWD against observations by comparing
 270 diagnostic quantities affected by GWs, such as upwelling (positive \bar{w}^*), Brünt-Väisälä frequency
 271 (N_B^2), and \bar{q}_ϕ (as shown in Figure 4). Near 80 km and equatorward of 30°N on 31 December, the
 272 eastward GWD (red contours in Figure 2d) is significantly stronger than the westward PW
 273 forcing (Figure 3a). Thus, the net wave forcing (from GWs and PWs) is eastward which helps to
 274 maintain the subtropical mesospheric jet core while driving an equatorward meridional
 275 circulation. The adjacent westward GWD on the poleward side also dominates the net wave
 276 forcing. By the end of December (Figure 2d), GWD became increasingly westward in the mid-

277 latitudes (with values exceeding $60 \text{ m}\cdot\text{s}^{-1}\cdot\text{day}^{-1}$) and concentrated near the zero-wind line. This
278 led to the wind shear increase evidenced by the constricted isotachs. The pronounced net
279 westward forcing would drive a poleward meridional circulation between 40° - 50°N . By
280 continuity, we would expect enhanced upwelling around 30° - 40°N just below $\sim 80 \text{ km}$.

281 **Figure 4a** shows the time-latitude evolution of GWD averaged between 0.2 hPa and 0.02
282 hPa, where strong GWD appears in Figures 2c and 2d. The formation of the double-maxima
283 wind structure on 31 December (vertical dashed line) occurs with the poleward movement of the
284 polar jet as represented by the dashed black contours. A strong westward GWD (blue regions)
285 persisted over the polar jet and followed its migration north. Eastward GWD began to dominate
286 the subtropics due to weakened underlying winds due to PW dampening noted in Figure 3. With
287 the SSW onset (vertical solid line), GWD eventually became eastward throughout NH due to the
288 underlying stratospheric wind reversal (De Wit et al., 2014). Figure 4b illustrates the
289 corresponding PW forcing in WACCM-SD at the same altitude range. Around 31 December, the
290 peak in westward PW acceleration between 30°N and 40°N corresponded with the formation of
291 the double maxima and is located between the subtropical (solid black contours) jet and the
292 slightly lower polar jet (dashed black contours). Comparing Figures 2d and 3a, peaks in eastward
293 GWD dominated PW forcing equatorward of 40°N near 0.02 hPa, locally accelerating the
294 subtropical jet. Regardless, the position and strength of westward PW acceleration between the
295 subtropical and polar jets in Figures 3a and 4b suggests that PWs are the driving mechanism for
296 the double-maxima wind configuration. The reason for PW deposition in this location may be
297 illuminated by further examining the background conditions.



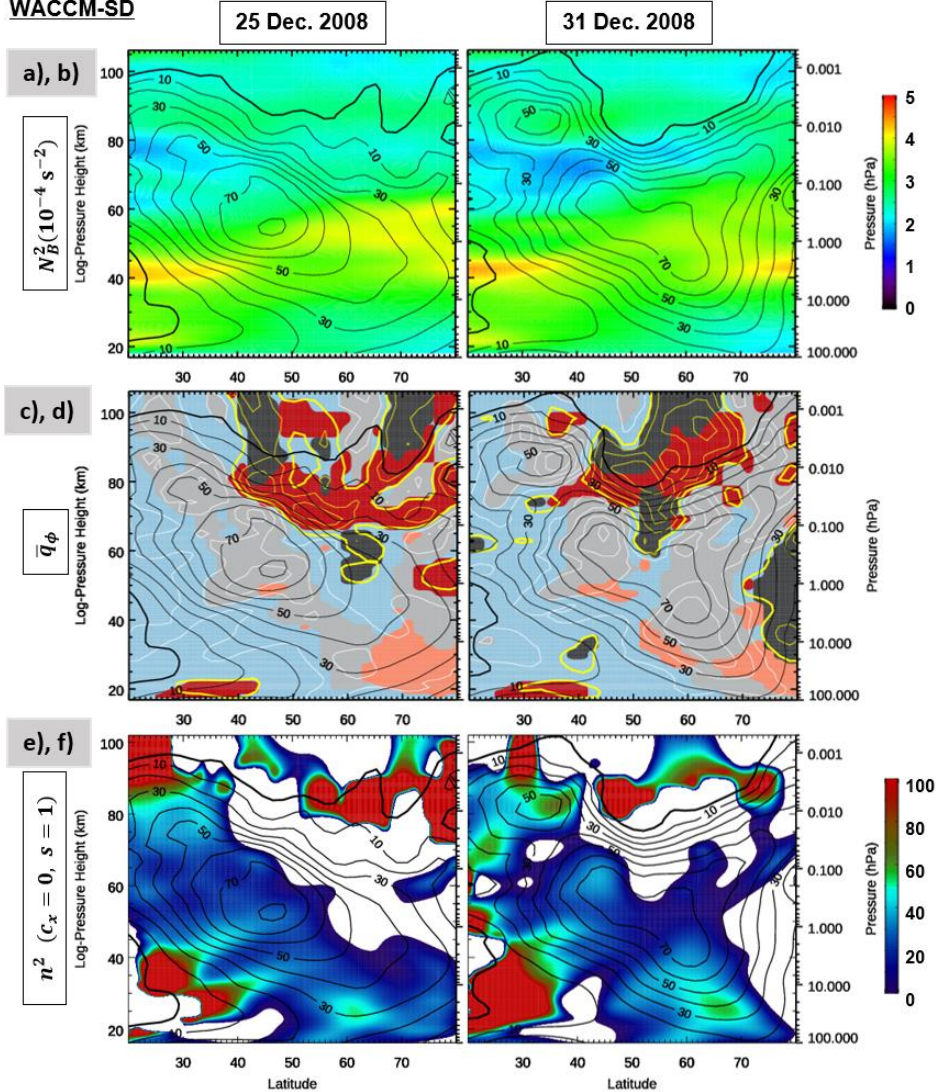
298
 299 **Figure 4.** Latitude-time sections from (a-e) WACCM-SD and (f-g) MLS averaged
 300 between 0.2 hPa and 0.02 hPa showing (a) GW drag, (b) PW acceleration, (c) upwelling or
 301 positive \bar{w}^* , (d, f) N_B^2 , and (e, g) nondimensionalized \bar{q}_ϕ . The \bar{u} values averaged from 1.0 to 0.1
 302 hPa indicates the polar jet (dashed contours). The \bar{u} values averaged from 0.1 to 0.01 hPa
 303 indicates the subtropical jet (solid contours). Vertical dashed line marks the formation of a
 304 double-maxima structure on 31 December 2008. Solid vertical line marks SSW onset on 22
 305 January 2009.

306 The enhanced upwelling expected around 31 December between 30°-40°N is seen in
 307 Figure 4c. The enhanced upwelling adiabatically cooled the subtropics, leading to a decrease in
 308 the vertical temperature gradient. This is evidenced by the corresponding decrease N_B^2 over the
 309 subtropics in both the model and observations (Figures 4d and 4f). For WACCM-SD, **Figures 5a**
 310 and 5b show the meridional structure of N_B^2 for 25 and 31 December. Over this time span, the

311 diminished N_B^2 region (in blue) between 70-80 km extended northward and became situated
 312 between double-maxima wind structure. The effect of adiabatic cooling on the stability of the
 313 atmosphere was investigated through \bar{q}_ϕ in Figures 4e and 4g. Generally, the sign changes in \bar{q}_ϕ
 314 occur at approximately 45°N and 65°N . With the double-maxima wind formation, \bar{q}_ϕ at high
 315 latitudes increases with the acceleration of the mesospheric wind (solid black contours). In
 316 WACCM-SD, the mesospheric zonal winds show high- and low-latitude maxima resembling a
 317 configuration conducive to instability between the latitudes of 45°N and 65°N (e.g., Orsolini &
 318 Simon, 1995).

Background Conditions

WACCM-SD



319

320

321

322

323

324

325

Figure 5. Altitude vs. latitude sections of (a, b) N_B^2 , (c,d) nondimensionalized \bar{q}_ϕ , and (e,f) nondimensionalized n^2 in WACCM-SD for 25 December 2008 (left column) and 31 December 2008 (right column). (c, d) White and yellow contours (every 1 unit) indicate positive and negative \bar{q}_ϕ respectively with the bold yellow contour indicating the zero value. In reference to the RHS of Equation 1, blue-, grey-, and red-shaded regions indicate the dominance of the first, second, and third term, respectively. Dark (light) colors represent a negative (positive)

326 contribution to \bar{q}_ϕ . Eastward \bar{u} is contoured every $10 \text{ m}\cdot\text{s}^{-1}$ as thin black contours, with the zero-
327 wind line thickened.

328 Figures 5c and 5d illustrate the nondimensionalized \bar{q}_ϕ and the relative dominance of
329 each RHS term in Equation 1. The positive and negative \bar{q}_ϕ values are contoured in white and
330 yellow, respectively. The negative \bar{q}_ϕ region is bounded by a bold yellow contour. Regions
331 where the magnitude of the beta term, barotropic term, and baroclinic term (RHS terms in
332 Equation 1) dominate are shown by the blue, grey, and red shading, respectively. Light and dark
333 tints of each color indicate whether the term is contributing positively (light) or negatively (dark)
334 to \bar{q}_ϕ . For example, since the planetary vorticity term is positive definite, the dominance of this
335 term is always represented as a light blue. With the development of the double-maxima wind
336 structure, positive \bar{q}_ϕ values developed well-organized cores (white contours), nearly collocated
337 with the local wind maxima. These enhanced values were dominated by the barotropic term
338 (grey region), reflecting the strong horizontal wind curvature and the tightening of the isotachs.
339 This enhanced wind shear was due to the strong westward GWD near the zero-wind line and the
340 adjacent eastward GWD (see Figure 2d). By the end of December, a valley of low \bar{q}_ϕ developed
341 between the local maxima extending diagonally from the poleward side of subtropical jet near 80
342 km, across to a negative pocket at 75 km and 30°N , and down to equatorward side of the polar
343 jet near 60 km. This valley between the local wind maxima was dominated by the baroclinic
344 term (shaded in dark red).

345 Equation 1 indicates that \bar{q}_ϕ depends also on N_B^2 through the baroclinic term. Assuming
346 other variables being fixed, a decrease in N_B^2 would diminish \bar{q}_ϕ . In comparing Figures 5a and
347 5b, strong vertical wind shear (evidenced by the tightened isotachs) coincides with a drastic
348 decline in N_B^2 . The decline in N_B^2 also coincides with the extension of the negative baroclinic
349 component (3rd term in Equation 1 that is dependent on N_B^2) in \bar{q}_ϕ into the subtropical
350 mesosphere. Therefore, the development of a double-maxima wind structure development led to
351 the lowered N_B^2 distribution and diminished \bar{q}_ϕ values.

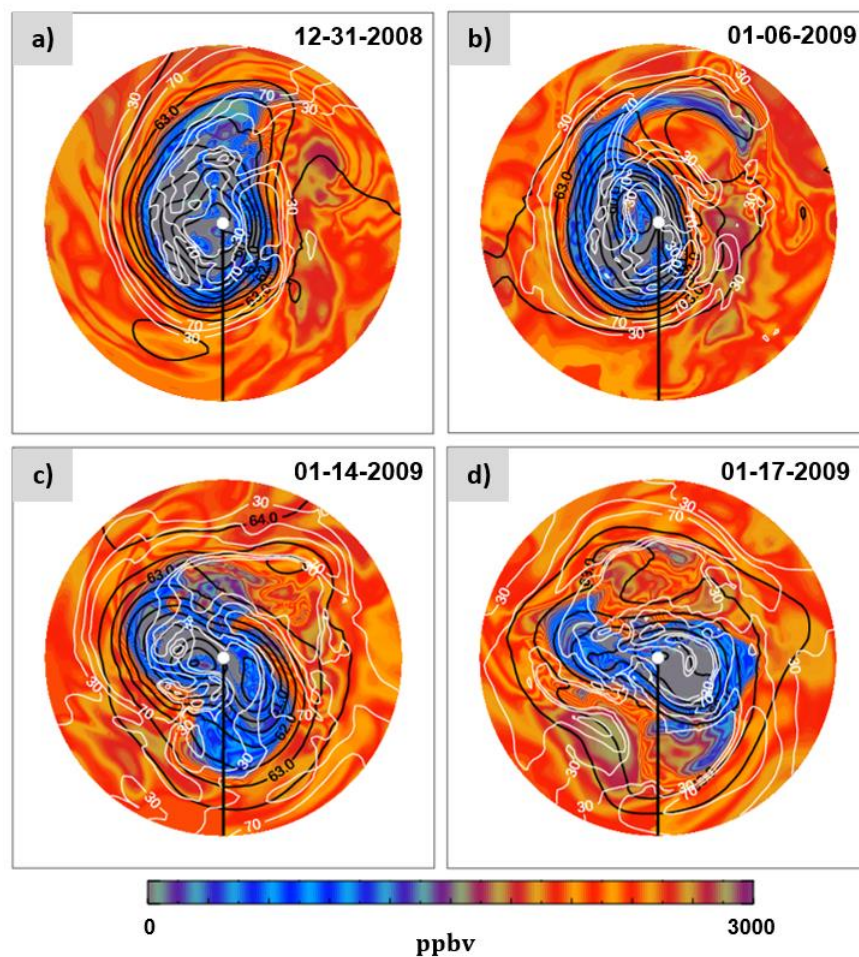
352 Furthermore, Equation 2 indicates that decreasing both N_B^2 and \bar{q}_ϕ would reduce the
353 squared refractive index (n^2) in the subtropics. For PWs propagating westward relative to the
354 flow, the reduction in refractive index can impact PW propagation and, ultimately, where PWs
355 deposit their energy upon dissipation. Figures 5e and 5f show the n^2 evolution for stationary PW
356 of zonal wavenumber 1. On 31 December, the aforementioned valley of low \bar{q}_ϕ (due to increased
357 wind shear) reduced n^2 and created pockets of wave evanescence (i.e., negative n^2). Moreover,
358 the enhanced (and positive) \bar{q}_ϕ seen in Figures 5c and 5d manifested as localized regions of large
359 n^2 .

360 Taken together, these changes in n^2 suggest a waveguide development that encourages
361 PWs to propagate toward the intervening region between the subtropical and polar jets (due to
362 enhanced n^2 at 44°N and 60 km). The negative n^2 pockets and diminished n^2 areas between the
363 jet cores (roughly $30\text{--}40^\circ\text{N}$ and 60-80 km) likewise limit PWs from further propagation. This is
364 supported by the strong PW EP flux convergence shown in Figure 3a. To this end, a positive
365 feedback loop was created promoting the separation of the jet cores. Increased PW forcing
366 assisted in upwelling (along with GWD). PW propagation was modulated by the enhanced
367 upwelling resulting in greater localized PW forcing. The increased wave forcing around the jet

368 cores also enhanced the vertical and horizontal curvature of the zonal winds and generated a
 369 more unstable flow (evidenced by growing evanescent regions in Figures 5e and 5f).

370 **Figure 6** illustrates the distribution of carbon monoxide (CO) which serves as a nearly
 371 conservative tracer to illuminate the horizontal flow evolution (e.g., Solomon et al., 1985). As
 372 discussed earlier, the juxtaposition of the evanescent and high n^2 region at 0.2 hPa in Figure 5f
 373 creates an ideal zone for PW dissipation. On 31 December (Figure 6a), a wavenumber-1
 374 perturbation appeared as a low-pressure region (evidenced by black geopotential height
 375 contours) equatorward, increasing the zonal wind (white contours) near the International Date
 376 Line. This distorted pattern helped form the subtropical mesospheric jet seen in Figures 2d and
 377 3a. By 6 January (Figures 6b), the vortex further deformed with features indicative of PW wave
 378 breaking; A filament of low CO (high potential vorticity) air was advected equatorward
 379 around 30°N, just poleward of the subtropical jet. This filament structure fostered the local meridional
 380 gradient reversal of the potential vorticity, that destabilized the flow. Notably, this wavenumber-
 381 1 pattern prior to a split SSW suggests that the dominant wavenumber associated with the
 382 formation of a double-maxima configuration does not necessarily coincide with that of the SSW
 383 event.

Polar Plots of CO Prior to SSW Onset at 0.1 hPa



384
 385
 386

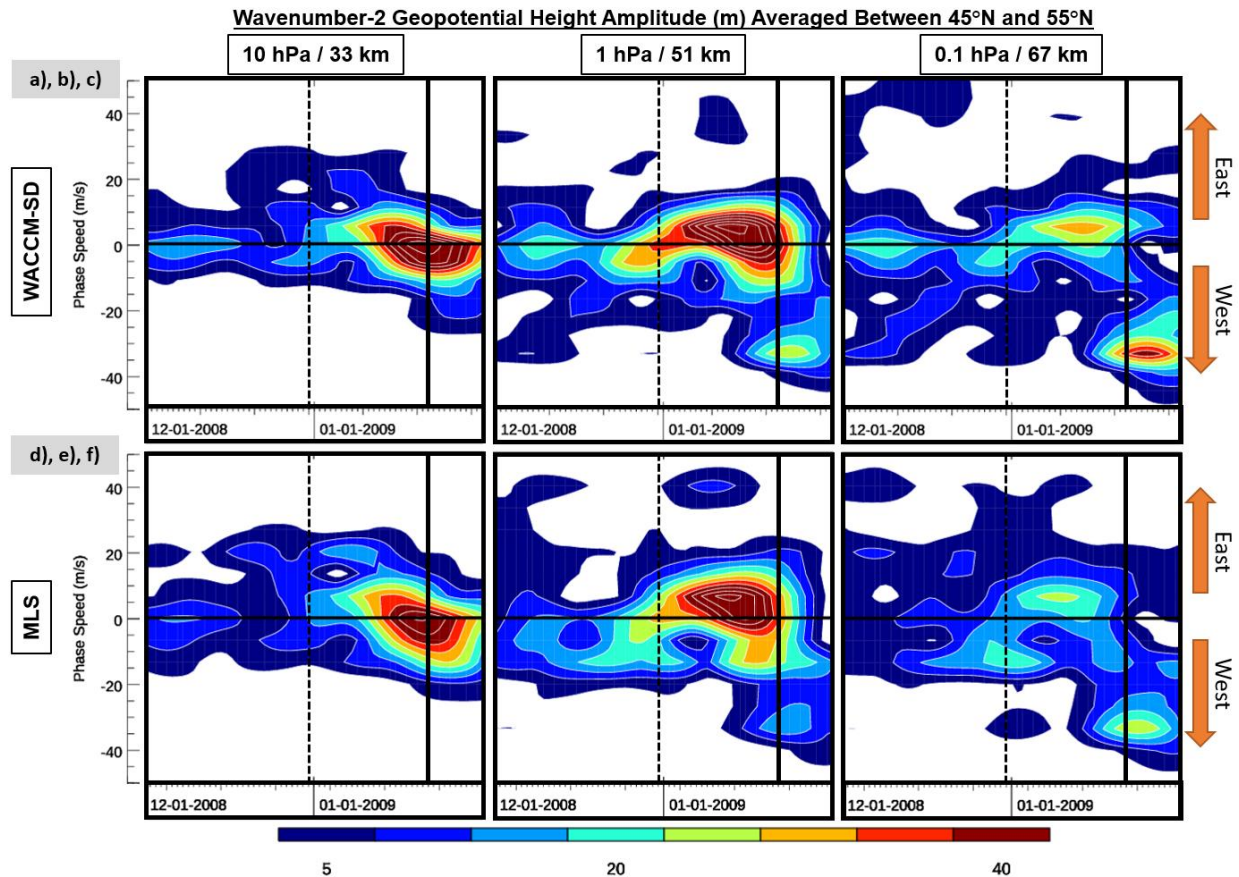
Figure 6. Stereographic polar projections of CO from WACCM-SD at 0.1 hPa. Geopotential height (black contours) is incremented by 0.5 km. Zonal wind isotachs of 30, 50,

387 and $70 \text{ m}\cdot\text{s}^{-1}$ are shown in white contours. The thick black vertical line depicts the Prime
388 Meridian.

389 In summary for this case study, the interplay between GWD and PW forcing resulted in a
390 double-maxima wind configuration. Both PWs and GWs deposited westward drag in the middle
391 to high latitudes. The upward transmittance of GWs that imposed strong eastward drag on the
392 subtropical mesosphere was ultimately modulated by underlying stratospheric winds due to PW
393 forcing. These three factors enhanced subtropical upwelling, leading to changes in N_B^2 through
394 adiabatic cooling. Thus, a positive feedback loop was created in which the double-maxima wind
395 configuration was promoted, and the mesospheric flow became more susceptible to shear
396 instability.

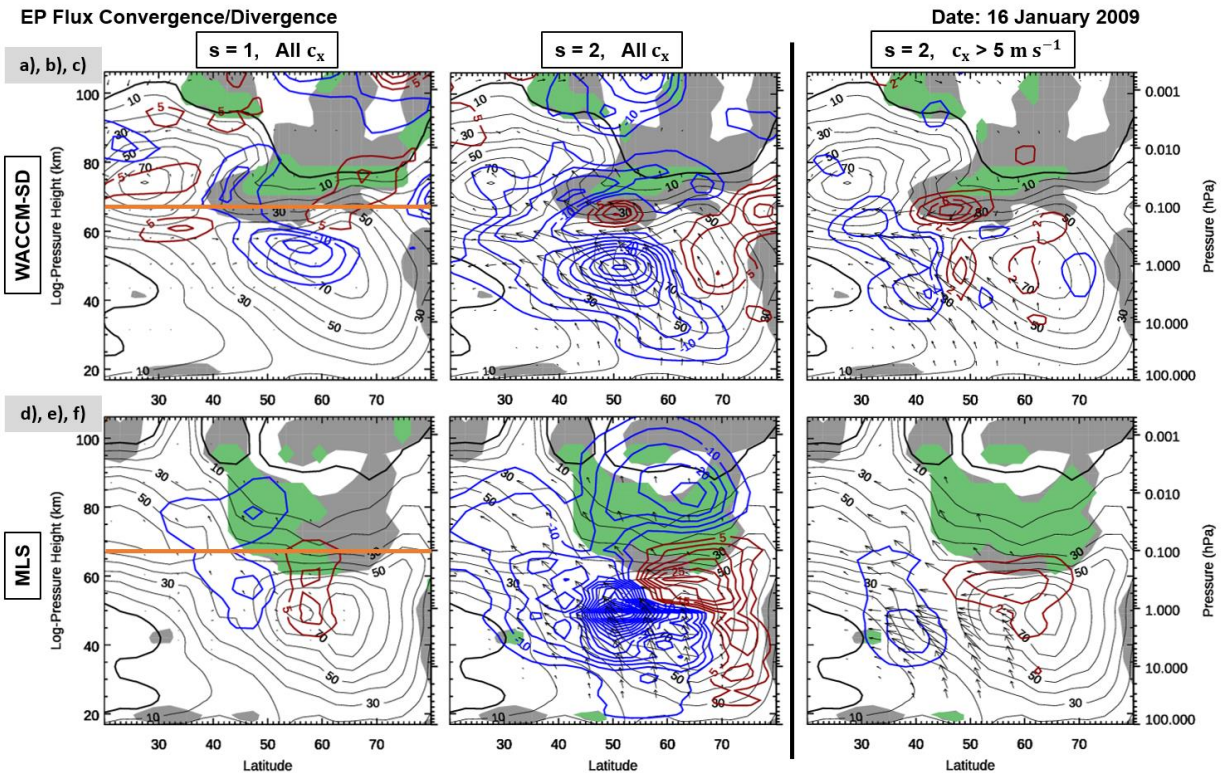
397 3.2 Emergence of EPWs and Instability

398 The development and persistence of the double-maxima wind structure prior to SSW
399 encouraged the generation of instability waves leading up to SSW onset. **Figure 6** shows the
400 polar plot at 0.1 hPa of carbon monoxide (CO) which serves as a long-lived tracer to illustrate
401 the evolving dynamics. By mid-January (Figures 6c and 6d), low CO air (bluish color) was
402 drawn towards the equator in a wavenumber-2 pattern as a result of two partially-separated low-
403 pressure systems. Between 14 and 17 January, the wavenumber-2 GHP slowly propagated
404 eastward. For both models and observations, **Figure 7** investigates the evolution of this pattern
405 by showing the wavenumber-2 GHP amplitude (averaged between 45°N and 55°N) as a function
406 of zonal phase speed and time. By the end of December, when the wind structure was in a
407 double-maxima configuration (dashed vertical line), the wave's phase speed distribution shifted
408 toward a mean eastward phase speed over a deep layer. The GHP amplitudes amplified
409 simultaneously and diminished with altitude. About 10 days before SSW onset, the wave
410 signatures peaked near $5 \text{ m}\cdot\text{s}^{-1}$ eastward phase speed. At 0.1 hPa, near the intervening level
411 between the two jet cores (c.f., Figure 5), Figures 7c and 7f show a similar slow eastward
412 propagation previously noted in the wavenumber-2 CO pattern of Figures 6c and 6d. After SSW
413 onset, a strong westward PW2 signature coincides with stratospheric wind reversal. Notably,
414 these westward-propagating PWs are instability waves that drive SSW recovery in the
415 mesosphere and lower thermosphere (Limpasuvan et al., 2016). Overall, the structure and
416 amplitude characteristics are remarkably similar between model and observations.



417
 418 **Figure 7.** Zonal phase speed vs. time plot of wavenumber-2 GHP amplitude (m) at 67 km
 419 averaged between 45°N and 55°N. White contours increment by 5 m·s⁻¹. Positive phase speed
 420 indicates eastward movement.

421 **Figures 8a,b,d,e** show the EP flux for wavenumber-1 and -2 PWs (PW1s and PW2s,
 422 respectively) of all phase speeds just prior to SSW onset (16 January 2009) in both the model
 423 (top row) and observations (bottom row). The observed and modeled double-maxima wind
 424 structure persisted from an earlier time in the winter (see Section 3.1). In both model and
 425 observations, an extensive region of negative \bar{q}_ϕ (grey-shaded area) appeared in a meridional
 426 local minimum of zonal-mean zonal wind near 0.1 hPa. The strong wind curvature responsible
 427 for a negative \bar{q}_ϕ is emphasized by the orange horizontal line in the Figures 8a and 8d crossing
 428 the same 30 m·s⁻¹ isotach twice. Consistent with the split polar vortex, PW2s dominated the
 429 wave flux activity. The observed PW2 activity (Figure 8e) showed one broad EP flux divergence
 430 region above the polar stratosphere while the simulated PW2 activity (Figure 8b) revealed two
 431 separate regions on the poleward and equatorward side of the polar jet. Areas of EP flux
 432 convergence (blue contours) appear mainly above and on the equatorward side of the polar jet.



433
 434 **Figure 8.** Altitude vs. latitude sections of PW1 (left column) and PW2 (middle column)
 435 for all phase speed, and for EPW2 (right column) as computed from WACCM-SD (top row) and
 436 MLS data (bottom row). Negative (blue) and positive (red) EP Flux divergence is contoured
 437 every $5 \text{ m}\cdot\text{s}^{-1}\cdot\text{day}^{-1}$, except for EPW2 where the contour interval is $2 \text{ m}\cdot\text{s}^{-1}\cdot\text{day}^{-1}$. Eastward \bar{u} is
 438 contoured every $10 \text{ m}\cdot\text{s}^{-1}$ as thin black contours, with the zero-wind line thickened in solid black.
 439 The negative \bar{q}_ϕ region is grey-shaded. The presence of a critical layer inside the negative \bar{q}_ϕ
 440 regions is shaded in green. The EP Flux vector components are scaled as done in Figure 3, but
 441 the EPW2 vector magnitudes are multiplied by 10.0.

442 We then elucidate EPWs by band-pass filtering for wavenumber-1 and wavenumber-2 PWs
 443 with eastward phase speed of $5 \text{ m}\cdot\text{s}^{-1}$ and greater. This phase speed was selected based the
 444 identified PW2 eastward peak in Figure 7. Considering the broad phase speed distribution in
 445 Figure 7, the derived EPW fluxes are expected to be smaller than the total PW fluxes with all
 446 phase speeds. Nevertheless, filtering minimizes the influence from upward-propagating quasi-
 447 stationary PWs and better illustrate the propagation and forcing instability PWs. The resulting
 448 EPW2 EP flux structures are shown in Figures 8c and 8f. In addition to an apparent source below
 449 the stratosphere, the EPW2 activity emerged from the edges of the negative \bar{q}_ϕ region with an
 450 overlying critical layer (green shading). The EPW2 EP flux vectors emanate from regions of
 451 EPW2 EP flux divergence (red contours) and overlap with the mid-latitude region of PW2 flux
 452 divergence (Figures 8b and 8e). The EP flux divergence suggests the localized EPW2 wave
 453 growth from instability. This growth occurred in eastward flow regime which indicates that these
 454 instability waves will have an eastward phase speed, as supported by the eastward shift in the
 455 phase speed distribution in Figure 7 around 16 January. The emanating EPW2 flux activity
 456 pointed equatorward toward a flux convergence region in the subtropics. Overall, the
 457 characteristics of these instability waves are consistent with wavenumber-2 eastward PWs
 458 identified by Coy et al. (2011) and Iida et al. (2014).

459

3.3 Instability Waves from an Over-reflection Perspective

460

461

462

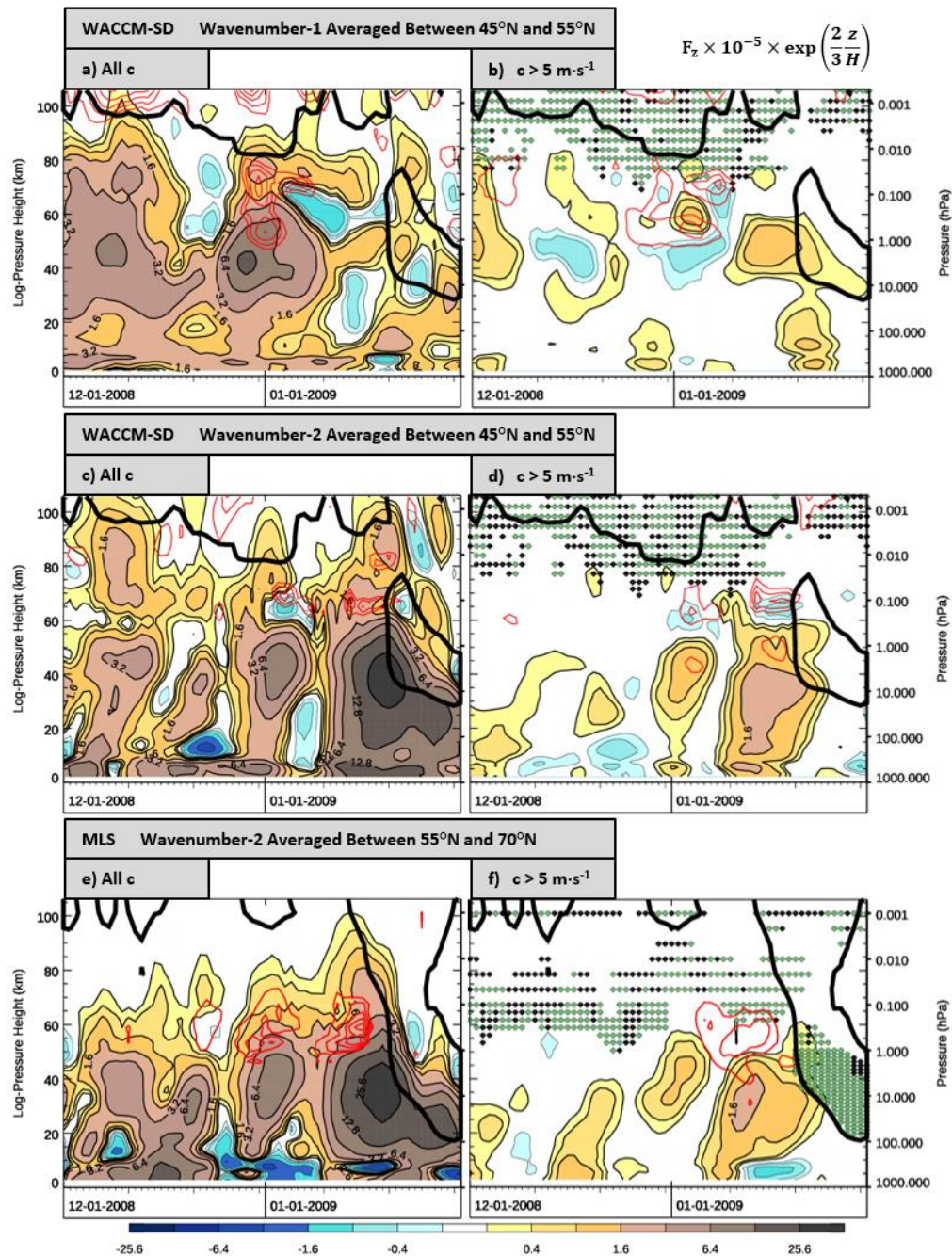
463

464

465

466

Figure 9 illustrates the altitude-time evolution of the vertical component of PW EP flux (upward in brown contours and downward in teal contours) and EP flux divergence (red contours) averaged between 45°N-55°N for WACCM-SD (Figures 9a,b,c,d) and 55°N to 70°N for MLS (Figures 9e and 9f). As noted by Coy et al. (2011), bursts of PW2 signal originating near the surface reached the 1-hPa level within days to weeks. Notably, WACCM-SD data shows consistently stronger vertical fluxes than MLS above 0.1 hPa and may account for the model wind bias at this higher altitude range.



467

468 **Figure 9.** Altitude vs. time showing vertical EP flux (filled-contours) of wavenumber-2
 469 disturbances for waves of (a, c) all phase speeds and (b, d) eastward phase speeds greater than 5
 470 $\text{m}\cdot\text{s}^{-1}$. Regular-sized (thin) black contours of $\pm 0.2 \times 2^m \text{ kg}\cdot\text{s}^{-2}$, $m \in [1,2,3,4,5,6,7,8]$ outline
 471 upward (downward) fluxes. Red contours show EP flux divergence and are incremented by (a, c)
 472 $5 \text{ m}\cdot\text{s}^{-1}\cdot\text{day}^{-1}$ and (b, d) $2 \text{ m}\cdot\text{s}^{-1}\cdot\text{day}^{-1}$. Thick black contour depicts the zero-wind line. Stippled
 473 regions shown in b and d also apply to a and c, respectively. Locations with negative \bar{q}_ϕ are
 474 marked by black stipples. Locations where a critical layer exists inside a region of negative \bar{q}_ϕ
 475 are marked by green stipples. Data sources and latitudinal averages are labeled at the top of each
 476 plot.

477 In Figures 9a,c,e, PWs exerted persistent eastward forcing (red contours) near 0.1 hPa
 478 around early and mid-January, coinciding with the incidental bursts of the underlying wave
 479 activity, also seen in Figures 8b and 8e. A burst of upward PW1 flux (Figure 9a) coincided with
 480 the formation of a double-maxima wind structure on 31 December. A deep layer (1.0 hPa to 0.02
 481 hPa) of PW growth, coinciding with a decrease vertical EP flux suggests PW1 instability. This
 482 formation of a PW1 eddy pattern was noted in Figures 6a and 6b at the same height. Figure 9b
 483 suggests that this instability results in some over-reflection as downward EPW1 EP flux (blue
 484 contours) is seen roughly below from a region of EPW1 divergence. Therefore, the double-
 485 maxima wind structure was ultimately created from the growth of a PW1 unstable mode.

486 Filtered for eastward phase speed greater than $5 \text{ m}\cdot\text{s}^{-1}$, Figures 9b and 9d show that
 487 EPW2 fluxes comprise some of the upward burst of PW2 but tend to be much weaker than the
 488 PW2. This is to be expected since the total PW2 has a broad range of phase speeds as suggested
 489 in Figure 7. After the formation of a double-maxima wind configuration, occurrences of PW2
 490 growth in the mesosphere (shown by EP flux divergence in Figures 9c and 9e) were evident
 491 suggesting instability. The eastward component of PW2 EP flux divergence (shown in Figures
 492 9d and 9f red contours) occurred below a critical layer that laid within a negative \bar{q}_ϕ region
 493 (green stipples).

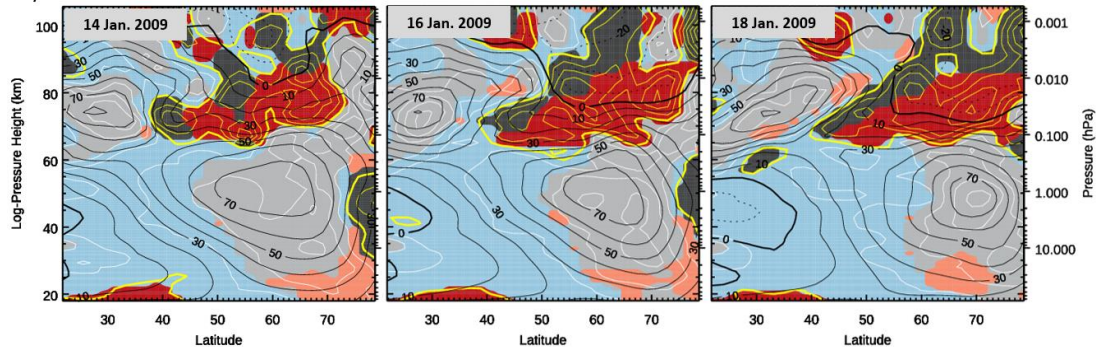
494 This configuration suggests EPW2 growth from over-reflection. This was particularly
 495 evident in the model (Figure 8c) as downward-pointing vectors emanated from a region of EPW2
 496 divergence. These downward-pointing vectors were not as evident in observations (Figure 8f),
 497 although the EPW2 group velocity was sharply diverted equatorward. Over-reflection is
 498 particularly evident in Figures 9c and 9d by the downward EP flux (blue areas) emanating from
 499 the region of wave growth at the beginning of January. The downward flux produced by other
 500 divergence regions may not be as evident as they may be masked by strong upward flux from
 501 tropospheric sources. The downward flux may also partially negate the upward flux, resulting in
 502 valleys between upward flux extrema.

503 As illustrated in Figure 1, instability wave can manifest as over-reflection and over-
 504 transmission as suggested by studies like Lindzen (1980) and Harnik & Heifetz (2007). Our
 505 study will regard the over-reflected and over-transmitted wave as the downward-propagating and
 506 upward-propagating component of the instability wave, respectively. However, unlike the
 507 idealized scenario, the over-reflected and over-transmitted waves have both vertical and
 508 meridional components in their group velocity (e.g., Figure 8).

509 This is expected since the negative \bar{q}_ϕ region consists of the relative contributions from
 510 the baroclinic and barotropic terms (in Equation 1), and these contributions vary in time as
 511 shown in Figures 5c and 5d during late December with the formation of the double-maxima wind

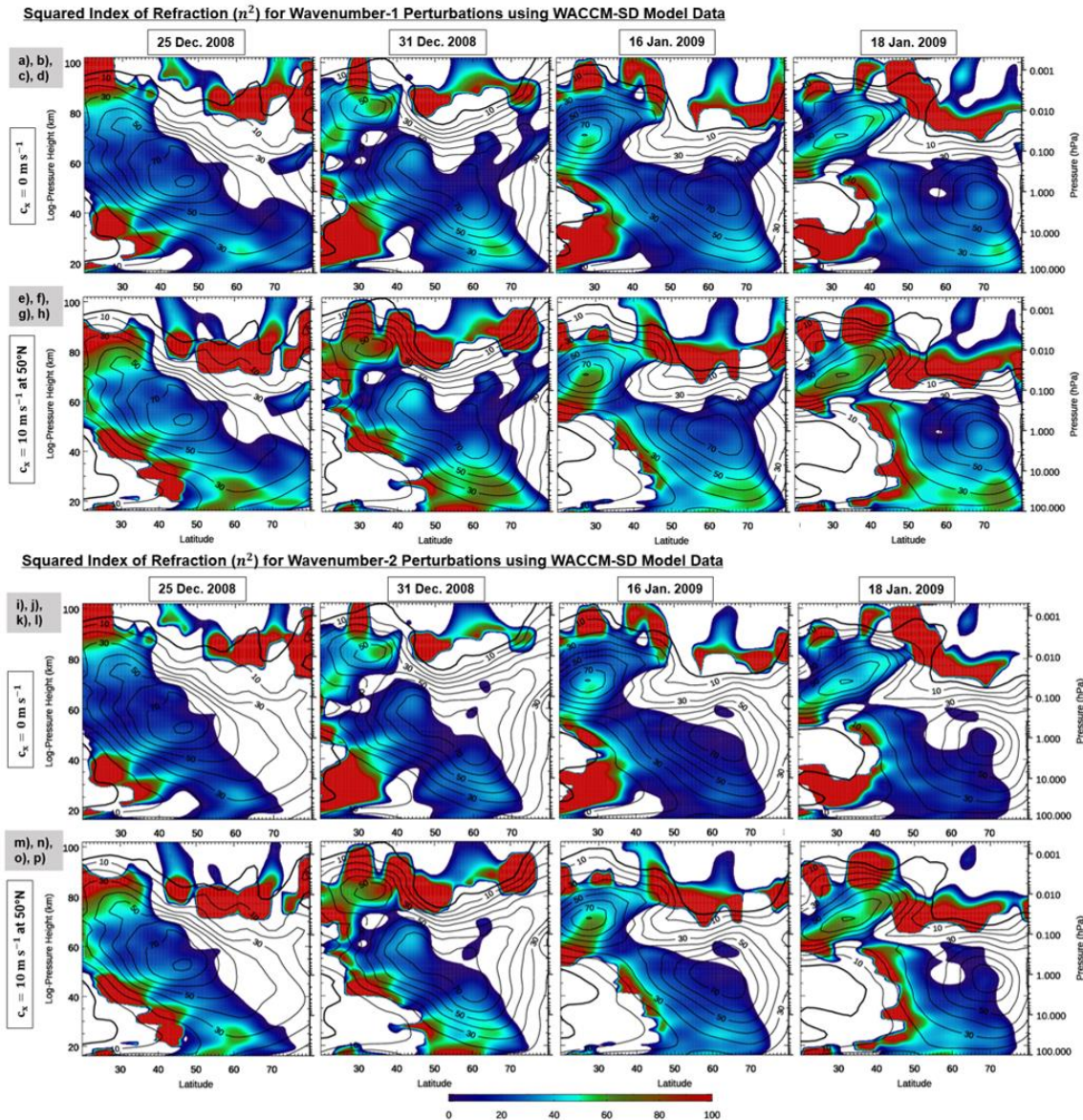
512 configuration. Thereafter, the negative \bar{q}_ϕ region (as shown in **Figure 10** within the yellow
 513 contours) became dominated by the baroclinic term (dark red) above the polar jet and the
 514 barotropic term (dark grey) on the poleward side of the subtropical jet. Above the polar jet, the
 515 dominance of the baroclinic term at high-latitudes would support a more vertical over-reflection
 516 while the dominance of the barotropic term at mid-latitudes (in the intervening region between
 517 the two jet cores) would support a more horizontal over-reflection. This mixing of baroclinic and
 518 barotropic contributions in the negative \bar{q}_ϕ region makes it difficult to identify instability waves
 519 simply from time-altitude sections (like Figure 9) if the instability EPW2 activity also propagate
 520 meridionally from the unstable region, as seen in Figures 8c and 8f.

\bar{q}_ϕ using WACCM-SD Model Data



521
 522 **Figure 10.** Altitude vs. latitude sections of nondimensionalized \bar{q}_ϕ . Plotting convention
 523 is like Figures 5c and 5d except at different times. Eastward \bar{u} is contoured every $10 \text{ m}\cdot\text{s}^{-1}$ as thin
 524 black contours, with the zero-wind line thickened.

525 Figure 10 shows that the two jet cores separated further as the polar jet migrated toward
 526 higher latitudes. This migration increased the meridional curvature of the zonal wind and thus
 527 increased \bar{q}_ϕ as evident by the maxima of white contours in Figure 10d at 1 hPa and 70°N . The
 528 increased \bar{q}_ϕ should coincide with an increase in the index of refraction (squared) n^2 as defined
 529 in Equation 2. **Figure 11** examines n^2 that supports the linear propagation of EPWs and, for
 530 contrast, of stationary PWs. For EPWs, the eastward phase speed of $10 \text{ m}\cdot\text{s}^{-1}$ is used in the
 531 n^2 computation. Consistent with the latitude band selected in Figures 9a-d, the reference latitude
 532 used in Equation 2 is 50°N . White areas represent wave evanescent regions with negative n^2
 533 values. Generally, the red regions correspond to extremely large n^2 values (>100), often
 534 occurring near critical layers.



535
 536 **Figure 11.** Squared refractive index, n^2 (color-filled contours) for PW1s (top) and PW2s
 537 (bottom) using WACCM-SD. For each row, PWs are specified by frequency and labeled in terms of
 538 phase speed (at a latitude if necessary) at the left of each row. Columns are organized by
 539 reference date. Eastward \bar{u} is contoured every $10 \text{ m}\cdot\text{s}^{-1}$ as thin black contours, with the zero-wind
 540 line thickened.

541 Significant change in n^2 occurred between 25 and 31 December that promotes the
 542 separation of the subtropical and polar jets through local PW dissipation. With the polar jet
 543 migrating northward thereafter, n^2 became more enhanced at higher winter latitudes throughout
 544 the stratosphere. This enhancement conditioned the background flow to guide PWs (originating
 545 in the mid-latitude troposphere) as well as EPWs more vertically near the edge of the polar
 546 vortex. Hence, a broad spectrum of PWs propagating from the lower stratosphere were more
 547 likely to reach the lower boundary of negative \bar{q}_ϕ (i.e., the turning level in Figure 1) and over-
 548 reflect. This likelihood is also seen in Figure 9 with the upward EP flux extending to higher
 549 altitude the double-maxima wind formation on 31 December. The vertical orientation of PWs

550 prior to SSW onset is common (e.g., Limpasuvan et al., 2012) and thus could explain why the
 551 appearance of EPWs have been noted, in particular, prior to SSWs as seen in Figure 9 (L. Coy et
 552 al., 2011; Iida et al., 2014).

553 Following the PW propagational path, the critical layer is absorptive if n^2 is positive
 554 approaching a critical layer. This is seen commonly on the subtropical side of the polar jet. If n^2
 555 is negative approaching the critical layer, then the critical layer would cap an evanescent region
 556 (like in Figure 1). In reference to Figure 1, over-transmitted waves would be actualized in the
 557 positive n^2 region above the critical layer, which is roughly 20 km thick for all plots in Figure
 558 11. Over-transmitted waves propagating from the critical layer can readily deposit their
 559 momentum creating a region of EP flux convergence (westward acceleration). This pattern is
 560 evident in Figure 8b and 8e as a region of PW2 EP flux divergence (red contours) juxtaposes
 561 with a region of EP flux convergence aloft (blue contours). When compared to n^2 for slow
 562 eastward waves on 16 January in Figure 11o, EP flux divergence occurred in the evanescent
 563 region while EP flux convergence occurred in a thin layer of positive n^2 aloft. As a result, the
 564 mesospheric zero-wind line descended (compare Figure 11o and 11p). The over-transmitted
 565 wave is not as evident for EPW2 on 16 January. However a small EP flux convergence near
 566 0.002 hPa and 45°N in the model (Figure 8c) and EP flux vectors emanating toward the same
 567 region in the observations (Figure 8f) suggest that the over-transmitted wave may deposit further
 568 equatorward near the subtropical jet. This is further investigated through a composite study in
 569 Section 4. For both wavenumber-1 and -2, the evanescent region becomes thinner approaching
 570 SSW onset. We note that the vertical geometry for instability idealized in Figure 1 is
 571 homomorphic with the meridional geometry (Lindzen, 1988). While the vertical geometry is the
 572 most evident in Figure 11, a similar meridional-oriented geometry could also encourage over-
 573 reflection.

574 In addition to suggesting the occurrence of over-reflection/over-transmission by EPW2,
 575 Figure 11 addresses why instability waves have a mean eastward phase speed. Assuming the
 576 upward-propagating PW signal with a distribution of phase speeds, the EPWs would experience
 577 a critical layer above the polar jet that is lower in altitude (see Equation 2). As a result, EPWs
 578 encounter a thinner evanescent layer giving them a greater capability to tunnel (given a large
 579 enough amplitude) and, consequentially, over-reflect as well as over-transmit.

580 3.4 Recap of the January 2009 SSW Case

581 In summary for this case study, the interplay between GWD and PW forcing resulted in a
 582 double-maxima wind configuration. Both PWs and GWs deposited westward drag in the middle
 583 to high latitudes. The upward transmittance of GWs that imposed strong eastward drag on the
 584 subtropical mesosphere was ultimately modulated by underlying stratospheric winds due to PW
 585 forcing. These three factors enhanced subtropical upwelling, leading to changes in N_B^2 through
 586 adiabatic cooling. Thus, a positive feedback loop was created in which the double-maxima wind
 587 configuration was promoted, and the mesospheric flow became more susceptible to shear
 588 instability.

589 The mesospheric EPWs reported by Coy et al. (2011) and Iida et al. (2014) prior to the
 590 January 2009 SSW appear to be manifestations of shear instability. Mesospheric PW2 growth
 591 occurred multiple times throughout the 2008-2009 winter. Each occurrence of wave growth
 592 coincided with upward-propagating PWs reaching the lower boundary of the negative \bar{q}_ϕ region.
 593 By isolating waves with eastward phase speeds greater than $5 \text{ m}\cdot\text{s}^{-1}$, it is shown that most of the

594 local acceleration due to instability waves came at the expense of a westward acceleration in the
 595 subtropical stratosphere. Over-reflection appears in conjunction with these instability waves and
 596 is supported by configuration of critical and turning levels. The evanescent region between the
 597 critical and turning levels became thinner approaching SSW onset, making over-reflection and
 598 over-transmission more likely. Concomitant to over-reflection, tunneling would allow PWs to
 599 extend (and dissipate) aloft.

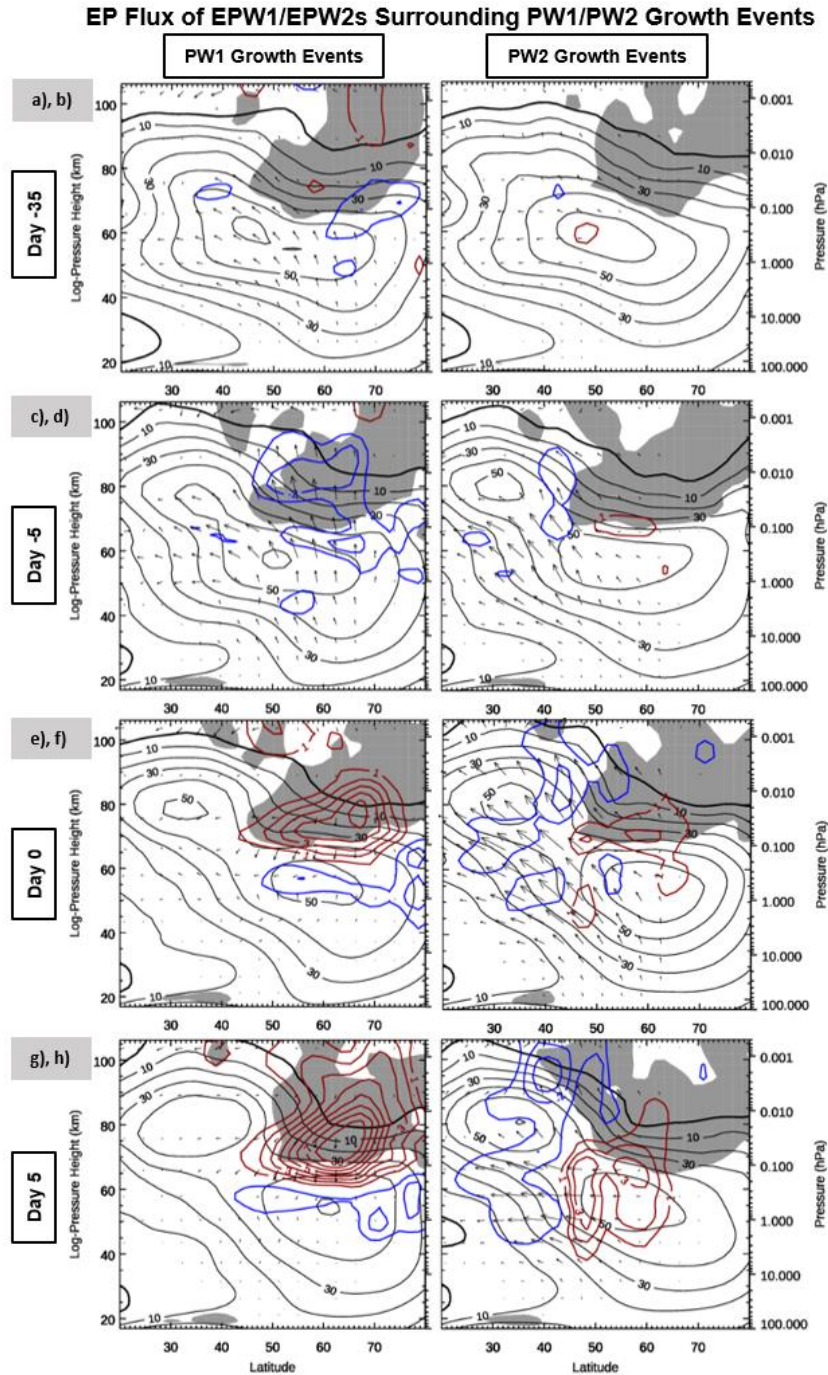
600 **4 Composite of EPWs**

601 A similar interplay between GWD and PW forcing is found prior to other SSWs as well
 602 (not shown). Thus, the evolution PW and GWD as well as the background wind are not unique
 603 to the often-studied January 2009 split SSW. Furthermore, after this double-maxima wind
 604 formation, instability EPWs were found to be associated with wavenumber-1 and wavenumber-2
 605 perturbations prior to SSWs with either split and displaced vortices. While instability waves are
 606 not necessarily dependent on a double-maxima wind configuration, strong and persistent
 607 occurrences of these instability waves were found after the formation of a double-maxima and
 608 prior to SSW. In all cases, these EPWs significantly impact the wind structure of the middle
 609 atmosphere. In some cases, EPWs can produce enough local eastward acceleration to generate a
 610 tertiary local maximum between the polar and subtropical jets.

611 Composites of mesospheric EPWs prior to SSW events (listed in Table 1) were
 612 developed to elucidate the robust behavior of EPWs in the mesosphere prior to SSW onset. As in
 613 the case studies, EPWs were isolated to better understand the propagation of instability waves
 614 (since they have a mean eastward phase speed) while filtering out much of the other upward-
 615 propagating PW signature (albeit not all of it). Since wavenumber-1 and -2 instability waves do
 616 not necessarily occur in tandem, separate composites were created to distinguish PW1 growth
 617 events from PW2 growth events. A PW1 growth event was defined to occur when the EPW1 EP
 618 flux divergence exceeds a critical value of $10 \text{ m}\cdot\text{s}^{-1}\cdot\text{day}^{-1}$ in the upper extension of the polar
 619 eastward jet (roughly between 30° - 80° N and 50-85 km) in close proximity to a negative
 620 \bar{q}_{ϕ} region and a critical layer. Since the wavenumber-2 growth signal tends to be weaker, a PW2
 621 growth event was selected when the EPW2 EP flux divergence exceeded $5 \text{ m}\cdot\text{s}^{-1}\cdot\text{day}^{-1}$ in that
 622 same region. The reference date (i.e., Day 0) of the respective event marks when the criteria for
 623 a growth event is fulfilled. As seen in Figure 9, EP flux divergence from EPW1 (Figure 9b) and
 624 EPW2 (Figure 9d) growth are not mutually exclusive, occurring irrespective of each other.

625 In total, 11 cases for PW1 growth events and 8 cases for the PW2 growth events were
 626 found. The identified dates (in YYYYMMDD format) for Day 0 for the PW1 events are
 627 19840206, 19841214, 19870102, 19890206, 19950115, 19971117, 20031206, 20051201,
 628 20090110, 20111228, 20121219. The dates for the PW2 events are 19841202, 19840211,
 629 19971212, 20031209, 20051223, 20090113, 20091229, 20121224. All growth events occur more
 630 than 8 days prior to an SSW onset. Given the broad phase speed range of associated with PW1
 631 and PW2 (suggested in Figure 7), these growth events identify the localized EPW1 and EPW2
 632 EP flux divergences suggestive of instability wave growth leading up to SSW onset. The
 633 composite was done after aligning each event on Day 0. As demonstrated in Figure 9d on 13
 634 December 2009, a region of EP flux divergence develops within a matter of 1-2 days. A change
 635 in critical value ($\pm 1\text{-}2 \text{ m}\cdot\text{s}^{-1}\cdot\text{day}^{-1}$) altered the Day 0 reference date of the PW growth event by
 636 roughly $\pm 1\text{-}2$ days. However, the composite results are largely unchanged.

637 **Figure 12** shows the meridional cross-sections of the composite EPW1 and EPW2 wave
638 activity, associated with the respective growth events. Well before the reference date (Day -35),
639 a local zonal-mean zonal wind maximum exists in the winter stratosphere defining the polar jet
640 core, similar to the climatology in Figure 2b. At this time, the EPW1 and EPW2 wave activities
641 are generally weak, especially for EPW2. Between Day -5 and Day 0, a double-maxima wind
642 structure develops (with a polar jet and subtropical jet). On Day -5, EPW1 and EPW2 activities
643 grow considerably with wave energy emanating from below, before being refracted toward the
644 subtropics near the stratopause. Some EPW1 activity continues to the top of the polar jet where
645 its flux convergence (blue contours) exerts westward forcing near the zero-wind line. By Day 0,
646 as expected from our composite criteria, we see a clear signature of wave growth. In particular,
647 the EPW1 flux divergence (red contours) exceeding $5 \text{ m}\cdot\text{s}^{-1}\cdot\text{day}^{-1}$ appears above the polar jet
648 core and adjacent to a relatively weaker flux convergence below. The EPW2 flux divergence
649 exceeding $2 \text{ m}\cdot\text{s}^{-1}\cdot\text{day}^{-1}$ appears above the polar jet core and flanked by areas of flux
650 convergence on the equatorward side. Thereafter, similar local eastward/westward forcing
651 pattern and wave activity continue to enhance as SSW onset approaches.



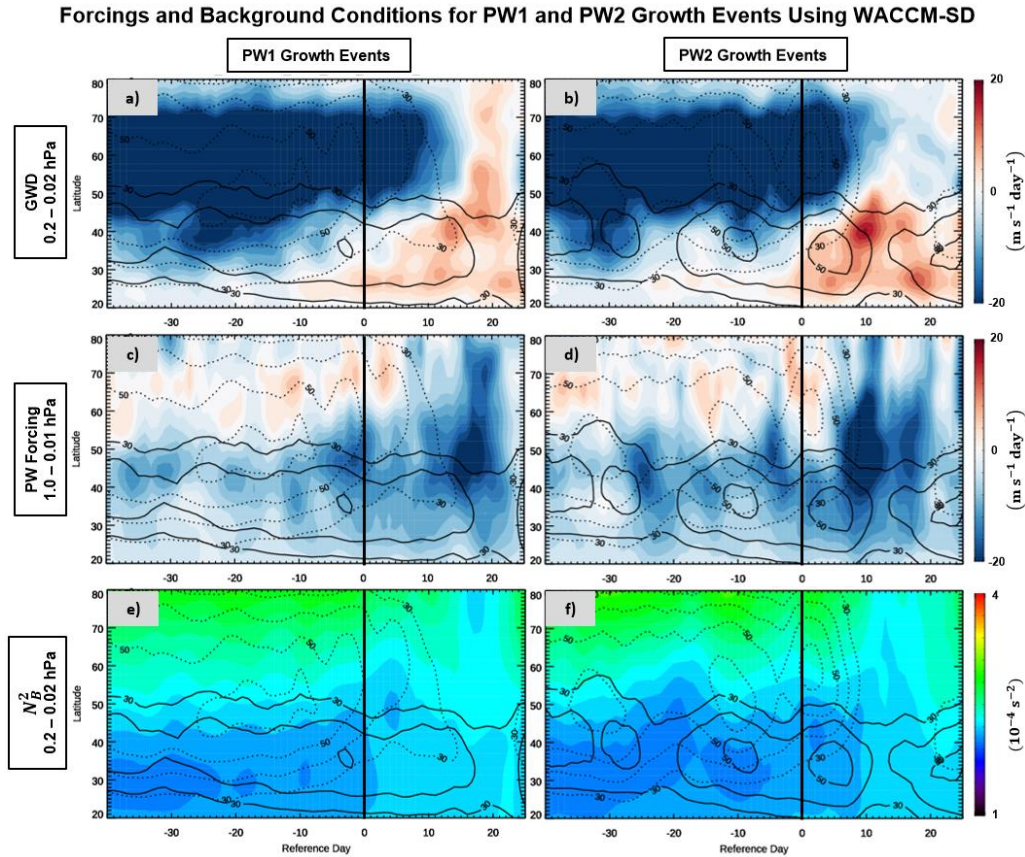
652
 653 **Figure 12.** Altitude vs. latitude composites for (a, c, e, g) PW1 growth events and (b, d, f,
 654 h) PW2 growth events (right column) on days specified at the left of each row. EP flux
 655 convergence (blue) and divergence (red) contours increment by $1 \text{ m} \cdot \text{s}^{-1} \cdot \text{day}^{-1}$. The EP Flux
 656 vector components are scaled as done in Figure 3. Grey areas show regions of negative
 657 composited \bar{q}_ϕ . Eastward \bar{u} is contoured every $10 \text{ m} \cdot \text{s}^{-1}$ as thin black contours, with the zero-
 658 wind line thickened.

659 The features of EPW growth indicate a robust “source-and-sink” structure for instability
 660 waves and over-reflection that is different between EPW1s and EPW2s. During PW1 growth

661 events, EPW1s grow in the high-latitude mesosphere (with EP flux divergence accelerating the
662 local flow) from an unstable region (grey shading) and emanate downward toward a region of EP
663 flux convergence. This instability wave activity and associated forcings tend to reduce the
664 vertical wind shear above the polar jet. On the other hand, EPW2s impose a more equatorward
665 local eastward acceleration on the upper extension of the polar jet, peaking once above the polar
666 jet and again in the intervening region between the two jet cores. Regardless, the development of
667 these waves stabilizes the double-maxima wind structure. The direction of the EP flux vectors
668 suggests that EPW2s (with a source above the polar jet) find their sink in the lower and poleward
669 extension of the subtropical jet. Considering the effect of zonal wavenumber on n^2 illustrated in
670 Figure 11, EPW1s would tend to propagate, and subsequently dissipate, further poleward than
671 EPW2 (due to the second term in Equation 2).

672 While the EPW1 over-reflection is evident on Days 0 and 5, the EP flux convergence
673 region associated with the accompanying over-transmitted wave is not evident. Large spatial
674 variation in EPW1 over-transmission may account for the negligible flux convergence. For PW2
675 growth events, the EPW2 flux convergence region on the poleward side of the subtropical jet
676 seems to indicate a more defined region for the dampening of over-transmitted waves.

677 The conditions leading up to these PW growth events were further investigated through
678 **Figure 13**. The polar jet (dashed black contours) deviates farther poleward from the subtropical
679 jet (solid black contours) approaching Day 0 (black vertical line) when the double-maxima wind
680 configuration fully develops (Figures 12e and 12f). Illustrated in Figures 13a and 13b, the GWD
681 pattern is similar to the 2009 SSW event (Figure 4a). During the double-maxima wind formation,
682 westward GWD accompanies the underlying polar jet's migration into high latitudes while
683 eastward GWD becomes dominant at lower latitudes. While not composited with respect to the
684 SSW onset, the illustrated poleward spreading of GWD and its eventual sign switch in the mid-
685 to high-latitude regions indicate an SSW onset roughly around days 10-20. Averaged between
686 0.1 and 0.01 hPa, the westward PW forcing becomes increasingly stronger between the polar and
687 subtropical jets as they separate (Figures 12c and 12d). The westward PW forcing eventually
688 maximizes and spreads throughout the winter hemisphere around SSW onset (days 10-20).

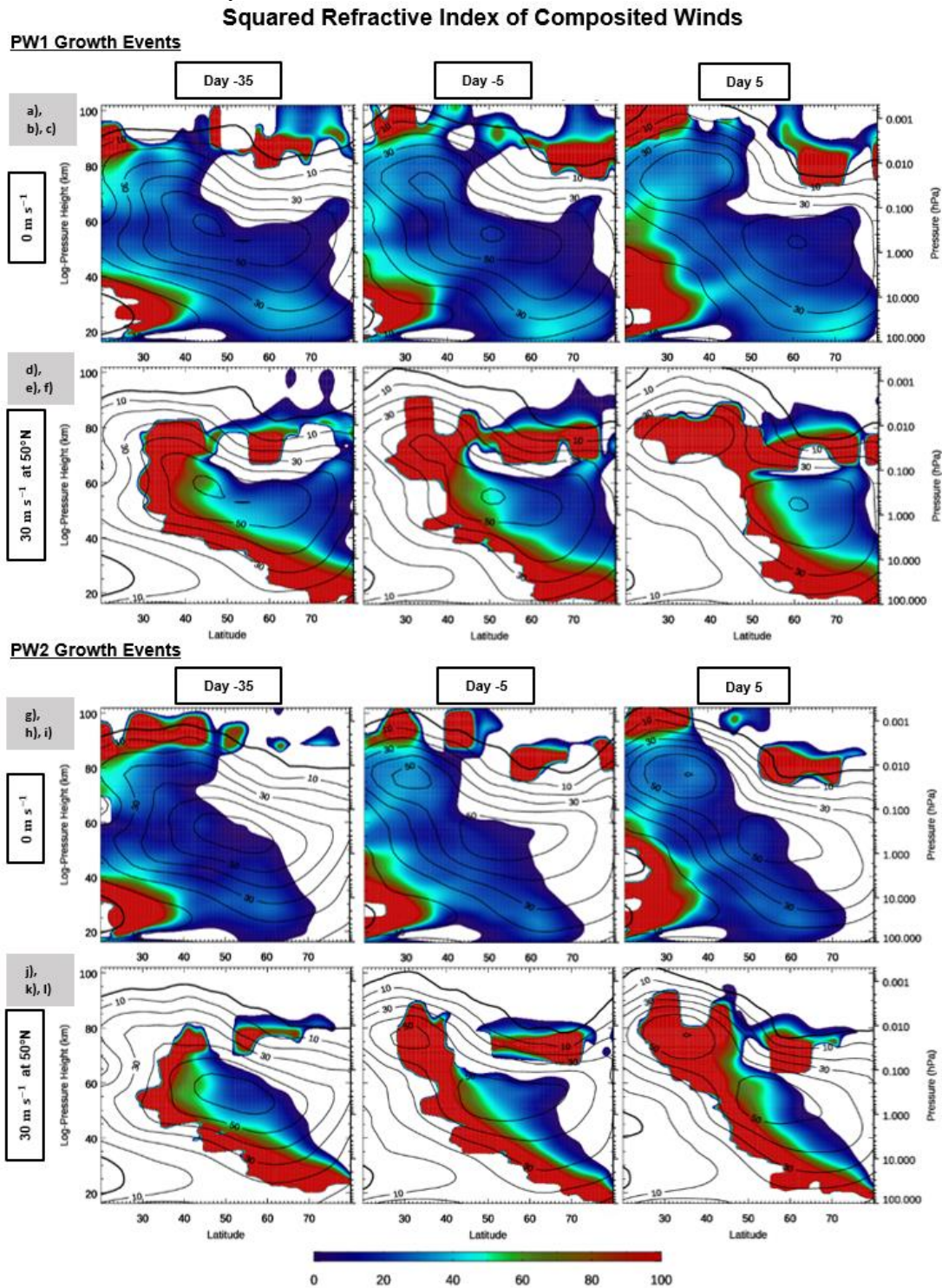


689
690 **Figure 13.** Latitude vs. time Day composites of (left column) PW1 and (right column) PW2
691 growth events showing. Variables and vertical averaging are indicated to the left of each row.
692 GW drag is calculated by summing parameterized GW drags and EP flux of wavenumbers
693 greater than 6. Zonal-mean zonal wind averaged from 1.0 to 0.1 hPa indicates the position and
694 strength of the polar jet (dashed contours) and the zonal-mean zonal wind averaged from 0.1 to
695 0.01 hPa indicates the position and strength of the subtropical jet (solid contours).

696 Akin to the 2009 SSW case (Figure 4), the net eastward forcing in the subtropical regions
697 would lead to localize upwelling and adiabatic cooling. These conditions accompany N_B^2
698 reduction (blue regions in Figures 13e and 13f) that eventually subside around days 10-20. For
699 both PW1 and PW2 growth events, the low N_B^2 region in the subtropics migrate poleward with
700 the polar jet and the PW dissipation. However, during the PW2 growth event, low values of N_B^2
701 migrate poleward twice over a period of ~ 15 days leading up to Day 0. These pulses of low N_B^2
702 migration coincide with pulses of strong zonal-mean zonal winds which may be unique to the
703 development of EPW2.

704 **Figure 14** shows n^2 for stationary and eastward PWs associated with the composited
705 wind structure for the PW1 growth event (top plots) and PW2 growth event (bottom plots).
706 While suggesting how the composited wind allows PW propagation, the illustration does not
707 illuminate the average PW propagation of individual events and associated wind. Accordingly,
708 the illustrated n^2 highlight the robust effect of a double-maxima wind configuration on PW
709 propagation. Like Figure 11, the reference latitude for a phase speed is set such that the n^2
710 evaluates the propagation path of a PW that retains its zonal wavenumber by changing in zonal

711 phase speed with latitude. A $30 \text{ m} \cdot \text{s}^{-1}$ eastward phase speed is chosen to emphasize the difference
 712 in the n^2 field for stationary and eastward PWs.



713 **Figure 14.** (a-f) PW1 and (g-l) PW2 growth event composite of the nondimensionalized
 714 squared refractive index (filled contours). For each row, PWs are specified by frequency and
 715 labeled in terms of phase speed (at a latitude if necessary) at the left of each row. Columns are
 716

717 organized by reference date. Eastward \bar{u} is contoured every $10 \text{ m}\cdot\text{s}^{-1}$ as thin black contours, with
 718 the zero-wind line thickened.

719 As suggested in Figure 13, the decrease in N_B^2 should lower n^2 and alter PW propagation.
 720 Comparing Day -35 to Day -5 in Figures 14a and 14b, n^2 decreases below the developing
 721 subtropical jet (around 60 km). For eastward PW1s (Figure 14e), n^2 turns negative here, creating
 722 an evanescent region and constricting the PW propagation path. For the PW2 growth event, the
 723 region of allowable PW propagation also shrinks. Overall, the composite shows the occurrence
 724 of the bottlenecking effect of n^2 between the newly formed polar jet and the subtropical jet that
 725 promote a region prone to PW deposition. Although not composited for the formation of a
 726 double-maxima wind structure, Figure 14 illustrates that the evolution of the background
 727 conditions that lead to shear instability appears consistent with the proposed mechanism
 728 separating the jets, as detailed for the 2009 SSW event (Section 3). In particular, two main
 729 regions of positive n^2 with opposite signs in \bar{q}_ϕ (see also Figure 12) are consistently present in
 730 mid- to upper-latitudes and separated by an evanescent region. Thus, a turning level is present
 731 with an evanescent region and critical layer aloft. These positive n^2 regions are well separated
 732 for stationary PWs poleward of 45°N by 10-20 km. However, the gap between these regions
 733 shrinks in time toward Day 0 when the PW flux divergence maximizes. Near the altitude of 70
 734 km, the gap is smallest around 55°N for PW2s and around 70°N for PW1s. This suggests that
 735 instability wave growth is associated with a thinning of the evanescent region.

736 Furthermore, PWs of higher eastward phase speeds tend to encounter a lower critical
 737 layer and a thinner evanescent region (as seen also in Figure 11). This shows that the wintertime
 738 middle atmosphere tends to over-reflect PWs with eastward phase speeds by Day 0 and shortly
 739 thereafter. Based on the localized westward acceleration (blue regions) on Day 5, Figure 12
 740 shows that over-reflection would increase the amount of deposition below the subtropical jet and
 741 at the pole. Since eastward waves can only exist in faster eastward background flows, they are
 742 more constrained in latitude and altitude than stationary and westward PWs. The westward
 743 accelerations by eastward-propagating instability waves would occur in regions where stationary
 744 and westward PWs can still propagate. Therefore, the eastward bias of the instability PWs allows
 745 them to be able to alter the propagation path for other PWs with more westward phase speeds.

746 5 Summary

747 This study examines the strong growth of the mesospheric EPWs prior to SSW events
 748 between 1980-2013. These events are associated with both split and displaced vortex.
 749 Previously, Coy et al. (2011) and Iida et al. (2014) reported their presence specifically for the
 750 2009 SSW event with a split vortex. With eastward zonal phase speed of $\sim 10 \text{ m}\cdot\text{s}^{-1}$, these EPWs
 751 are attributed to shear instability between the double-maxima eastward wind configuration,
 752 characterized by the subtropical mesospheric wind maximum and a polar stratospheric jet core.
 753 Such wind structure emerged from the interactions between GWD and PW forcing. Preceding
 754 the formation of this double-maxima wind configuration was the presence of subtropical
 755 eastward GWD adjacent to the mid- to high-latitude westward GWD in the mesosphere. This
 756 distinctive GWD pattern induced a subtropical upwelling that locally lowered N_B^2 and \bar{q}_ϕ . The
 757 resultant change in n^2 further promoted the separation of the polar and subtropical jets by
 758 directing PW damping toward the intervening region between the wind maxima. Our study
 759 shows that the formation of double-maxima wind structure during the 2008-2009 winter
 760 manifests as the growth of an unstable PW1.

761 The background flow evolution leading to SSW onset fostered wave geometry suitable
762 for wave over-reflection (c.f., Figure 1). With the formation of a double-maxima wind structure,
763 the polar jet core strengthened and migrated poleward as the wave evanescent layer around 0.01
764 hPa (seen in Figure 11) became thinner. The stronger polar jet guided the upward-propagating
765 PWs (see Figures 10 and 11) more vertically toward the thin evanescent region, increasing the
766 likelihood of over-reflection, particularly for EPWs. Notably, this polar wind evolution may also
767 provide the background wave geometry to favor SSW onset through resonance (e.g., Albers &
768 Birner, 2014).

769 The composite evolution of EPW1 and EPW2 revealed their growth in parallel with the
770 double-maxima wind configuration (see Figure 12). Local eastward accelerations due to flux
771 divergence near their wave sources generally occurred above the polar jet. Accompanied by
772 westward acceleration, the damping of EPW1 appeared on the equatorward and poleward side of
773 the polar jet core. In contrast, EPW2 damping led to westward acceleration on the poleward
774 flank of the subtropical jet.

775 EPWs appear to be mesospheric instability waves with overlapping characteristics of
776 over-reflection of upward-propagating PWs. While suitable wave geometry for over-reflection
777 exists throughout the winter, a double-maxima wind configuration increases the likelihood of
778 over-reflection. In reducing the preexisting wind shear and, thereby, stabilizing the polar jet,
779 EPWs can significantly impact the jet structure and may play a key role in the nature and timing
780 of SSW events.

781 Acknowledgments

782 CR is supported by funding from the National Science Foundation (NSF) awards (RUI
783 1642232; REU 1560210). VL is supported by NSF Intergovernmental Panel Agreement. YO is
784 supported in part by the Research Council of Norway/CoE under contract 223252/F50. The
785 authors acknowledge the computing and technical support from the NCAR Computation
786 Information Systems Laboratory as well as the Coastal Carolina University cyberinfrastructure
787 (CCU CI) project, funded in part by NSF award MRI 1624068. The relevant daily model output
788 can be accessed through the CCU CI at <https://mirror.coastal.edu/sce>. The MLS temperature and
789 geopotential height data can be retrieved from <https://doi.org/10.5067/Aura/MLS/DATA2520>
790 and <https://doi.org/10.5067/Aura/MLS/DATA2507>, respectively.

791 References

- 792 Albers, J. R., & Birner, T. (2014), Vortex Preconditioning due to Planetary and Gravity Waves
793 prior to Sudden Stratospheric Warmings. *Journal of the Atmospheric Sciences*, 71, 4028–
794 4054. <https://doi.org/10.1175/JAS-D-14-0026.1>
- 795 Andrews, D. G., Holton, J. R., & Leovy, C. B. (1987), *Middle Atmosphere Dynamics*. San
796 Diego, California: Academic Press.
- 797 Baldwin, M. P., & Dunkerton, T. J. (2001), Stratospheric harbingers of anomalous weather
798 regimes. *Science*, 294, 581–584. <https://doi.org/10.1126/science.1063315>
- 799 Butler, A. H., Seidel, D. J., Hardiman, S. C., Butchart, N., Birner, T., & Match, A. (2015),
800 Defining sudden stratospheric warmings. *Bulletin of the American Meteorological Society*,
801 (November), 1913–1928. <https://doi.org/10.1175/BAMS-D-13-00173.1>

- 802 Chandran, A., Garcia, R. R., Collins, R. L., & Chang, L. C. (2013), Secondary planetary waves
803 in the middle and upper atmosphere following the stratospheric sudden warming event of
804 January 2012. *Geophysical Research Letters*, *40*, 1861–1867.
805 <https://doi.org/10.1002/grl.50373>
- 806 Charlton, A. J., & Polvani, L. M. (2007), A New Look at Stratospheric Sudden Warmings. Part I:
807 Climatology and Modeling Benchmarks. *J. Climate*, *20*, 470–488.
808 <https://doi.org/10.1175/JCLI3994.1>
- 809 Charney, J. G., & Eliassen, A. (1949), A Numerical Method for Predicting the Perturbations of
810 the Middle Latitude Westerlies. *Tellus*, *1*, 38–54. <https://doi.org/10.3402/tellusa.v1i2.8500>
- 811 Coy, L., Eckermann, S. D., Hoppel, K. W., & Sassi, F. (2011), Mesospheric Precursors to the
812 Major Stratospheric Sudden Warming of 2009: Validation and Dynamical Attribution Using
813 a Ground-to-Edge-of-Space Data Assimilation System. *Journal of Advances in Modeling
814 Earth Systems*, *3*, 1–7. <https://doi.org/10.1029/2011MS000067>
- 815 Coy, Lawrence, & Pawson, S. (2015), The major stratospheric sudden warming of January 2013:
816 Analyses and forecasts in the GEOS-5 data assimilation system. *Monthly Weather Review*,
817 *143*, 491–510. <https://doi.org/10.1175/MWR-D-14-00023.1>
- 818 Dickinson, R. E. (1973), Baroclinic Instability of an Unbounded Zonal Shear Flow in a
819 Compressible Atmosphere. *J. Atmos. Sci.*, *30*, 1520–1527.
- 820 Duck, T. J., Whiteway, J. A., & Carswell, A. I. (2001), The Gravity Wave–Arctic Stratospheric
821 Vortex Interaction. *Journal of the Atmospheric Sciences*, *58*(23), 3581–3596.
822 [https://doi.org/10.1175/1520-0469\(2001\)058<3581:TGWASV>2.0.CO;2](https://doi.org/10.1175/1520-0469(2001)058<3581:TGWASV>2.0.CO;2)
- 823 Ern, M., Preusse, P., Alexander, M. J., & Warner, C. D. (2004), Absolute values of gravity wave
824 momentum flux derived from satellite data. *Journal of Geophysical Research D:
825 Atmospheres*, *109*(20), 1–17. <https://doi.org/10.1029/2004JD004752>
- 826 Fetzer, E. J., & Gille, J. C. (1994), Gravity Wave Variance in LIMS Temperatures. Part I:
827 Variability and Comparison with Background Winds. *Journal of the Atmospheric Sciences*.
828 [https://doi.org/10.1175/1520-0469\(1994\)051<2461:gwvilt>2.0.co;2](https://doi.org/10.1175/1520-0469(1994)051<2461:gwvilt>2.0.co;2)
- 829 Gelaro, R., McCarty, W., Suárez, M. J., Todling, R., Molod, A., Takacs, L., et al. (2017), The
830 modern-era retrospective analysis for research and applications, version 2 (MERRA-2).
831 *Journal of Climate*, *30*, 5419–5454. <https://doi.org/10.1175/JCLI-D-16-0758.1>
- 832 Goncharenko, L. P., Chau, J. L., Liu, H. L., & Coster, A. J. (2010), Unexpected connections
833 between the stratosphere and ionosphere. *Geophysical Research Letters*, *37*(L10101).
834 <https://doi.org/10.1029/2010GL043125>
- 835 Harada, Y., Goto, A., Hasegawa, H., Fujikawa, N., Naoe, H., & Hirooka, T. (2010), A major
836 stratospheric sudden warming event in January 2009. *Journal of the Atmospheric Sciences*,
837 *67*, 2052–2069. <https://doi.org/10.1175/2009JAS3320.1>
- 838 Harnik, N., & Heifetz, E. (2007), Relating overreflection and wave geometry to the
839 counterpropagating Rossby wave perspective: Toward a deeper mechanistic understanding
840 of shear instability. *Journal of the Atmospheric Sciences*, *64*, 2238–2261.
841 <https://doi.org/10.1175/JAS3944.1>
- 842 Hartmann, D. L. (1983), Barotropic Instability of the Polar Night Jet Stream. *J. Atmos. Sci.*

- 843 [https://doi.org/10.1175/1520-0469\(1983\)040%3C0817:BIOTPN%3E2.0.CO;2](https://doi.org/10.1175/1520-0469(1983)040%3C0817:BIOTPN%3E2.0.CO;2)
- 844 Iida, C., Hirooka, T., & Eguchi, N. (2014), Circulation changes in the stratosphere and
845 mesosphere during the stratospheric sudden warming event in January 2009. *Journal of*
846 *Geophysical Research*, *119*, 7104–7115. <https://doi.org/10.1002/2013JD021252>
- 847 Kuttippurath, J., & Nikulin, G. (2012), A comparative study of the major sudden stratospheric
848 warmings in the Arctic winters 2003/2004–2009/2010. *Atmospheric Chemistry and Physics*,
849 *12*, 8115–8129. <https://doi.org/10.5194/acp-12-8115-2012>
- 850 Leovy, C. (1964), Simple models of thermally driven mesospheric circulation. *Journal of*
851 *Atmospheric Sciences*, *21*(4), 327–341.
- 852 Leovy, C. B., & Webster, P. J. (1976), Stratospheric long waves - Comparison of thermal
853 structure in the Northern and Southern Hemispheres. *Journal of Atmospheric Sciences*, *33*,
854 1624–1638. [https://doi.org/doi:10.1175/1520-0469\(1976\)033<1624:SLWCOT>2.0.CO;2](https://doi.org/doi:10.1175/1520-0469(1976)033<1624:SLWCOT>2.0.CO;2)
- 855 Limpasuvan, V., Richter, J. H., Orsolini, Y. J., Stordal, F., & Kvissel, O. K. (2012), The roles of
856 planetary and gravity waves during a major stratospheric sudden warming as characterized
857 in WACCM. *Journal of Atmospheric and Solar-Terrestrial Physics*, *78–79*, 84–98.
858 <https://doi.org/10.1016/j.jastp.2011.03.004>
- 859 Limpasuvan, V., Orsolini, Y. J., Chandran, A., Garcia, R. R., & Smith, A. K. (2016), On the
860 composite response of the MLT to major sudden stratospheric warming events with
861 elevated stratopause. *Journal of Geophysical Research*, *121*, 4518–4537.
862 <https://doi.org/10.1002/2015JD024401>
- 863 Lindzen, R. S., Farrell, B., & Tung, K. K. (1980), The concept of wave overreflection and its
864 application to baroclinic instability. *Journal of the Atmospheric Sciences*, *37*, 44–63.
865 [https://doi.org/10.1175/1520-0469\(1980\)037<0044:TCOWOA>2.0.CO;2](https://doi.org/10.1175/1520-0469(1980)037<0044:TCOWOA>2.0.CO;2)
- 866 Lindzen, Richard S. (1988), Instability of Plane Parallel Shear Flow. *Pageoph*, *126*(1), 103–121.
- 867 Livesey, N. J., Read, W. G., Wagner, L. F., Lambert, A., Manney, G. L., Valle, L. F. M., et al.
868 (2017), *Earth Observing System (EOS) Microwave Limb Sounder (MLS) Version 4.2x Level*
869 *2 data quality and description document. JPL D-33509 Rev. D*. Pasadena, California: Jet
870 Propulsion Laboratory, California Institute of Technology.
- 871 Manney, G. L., Krüger, K., Pawson, S., Minschwaner, K., Schwartz, M. J., Daffer, W. H., et al.
872 (2008), The evolution of the stratopause during the 2006 major warming: Satellite data and
873 assimilated meteorological analyses. *Journal of Geophysical Research*, *113*(D11115), 1–16.
874 <https://doi.org/10.1029/2007jd009097>
- 875 Manney, G. L., Schwartz, M. J., Krüger, K., Santee, M. L., Pawson, S., Lee, J. N., et al. (2009),
876 Aura Microwave Limb Sounder observations of dynamics and transport during the record-
877 breaking 2009 Arctic stratospheric major warming. *Geophysical Research Letters*, *36*(12),
878 1–5. <https://doi.org/10.1029/2009GL038586>
- 879 Manny, G. L., Nathan, T. R., & Stanford, J. L. (1988), Barotropic stability of realistic
880 stratospheric jets. *Journal of Atmospheric Sciences*, *45*(18), 2545–2555.
- 881 Marsh, D. R., Mills, M. J., Kinnison, D. E., Lamarque, J. F., Calvo, N., & Polvani, L. M. (2013),
882 Climate change from 1850 to 2005 simulated in CESM1(WACCM). *Journal of Climate*, *26*,
883 7372–7391. <https://doi.org/10.1175/JCLI-D-12-00558.1>

- 884 Matsuno, T. (1971), A dynamical model of stratospheric sudden warming. , 1479–1494.
885 Retrieved from [http://journals.ametsoc.org/doi/pdf/10.1175/1520-](http://journals.ametsoc.org/doi/pdf/10.1175/1520-0469%281971%29028%3C1479%3AADMOTS%3E2.0.CO%3B2)
886 [0469%281971%29028%3C1479%3AADMOTS%3E2.0.CO%3B2](http://journals.ametsoc.org/doi/pdf/10.1175/1520-0469(1971)29:028<1479:ADMOTS>2.0.CO;2)
- 887 Matthias, V., & Ern, M. (2018), On the origin of the mesospheric quasi-stationary planetary
888 waves in the unusual Arctic winter 2015/2016. *Atmospheric Chemistry and Physics*, 18(7),
889 4803–4815. <https://doi.org/10.5194/acp-18-4803-2018>
- 890 O’Neill, A., & Youngblut, C. E. (1982), Stratospheric Warmings Diagnosed Using the
891 Transformed Eulerian-Mean Equations and the Effect of the Mean State on Wave
892 Propagation. *Journal of the Atmospheric Sciences*, 39, 1370–1386.
893 [https://doi.org/10.1175/1520-0469\(1982\)039<1370:swdutt>2.0.co;2](https://doi.org/10.1175/1520-0469(1982)039<1370:swdutt>2.0.co;2)
- 894 Orsolini, Y., & Simon, P. (1995), Idealized life cycles of planetary-scale barotropic waves in the
895 middle atmosphere. *Journal of the Atmospheric Sciences*, 52(22), 3817–3835.
- 896 Pedatella, N. M., Oberheide, J., Sutton, E. K., Liu, H., Anderson, J. L., & Raeder, K. (2016),
897 Journal of Geophysical Research : Space Physics Short-term nonmigrating tide variability in
898 the mesosphere , thermosphere , and ionosphere. *Journal of Geophysical Research: Space*
899 *Physics*, 121, 3621–3633. <https://doi.org/10.1002/2016JA022528>.Received
- 900 Pedlosky, J. (1987), *Geophysical Fluid Dynamics*. (2nd ed.). New York: Springer.
- 901 Richter, J. H., Sassi, F., & Garcia, R. R. (2010), Toward a Physically Based Gravity Wave
902 Source Parameterization in a General Circulation Model. *Journal of the Atmospheric*
903 *Sciences*, 67, 136–156. <https://doi.org/10.1175/2009JAS3112.1>
- 904 Rüfenacht, R., Baumgarten, G., Hildebrand, J., Schranz, F., Matthias, V., Stober, G., et al.
905 (2018), Intercomparison of middle-atmospheric wind in observations and models.
906 *Atmospheric Measurement Techniques*, 11, 1971–1987. [https://doi.org/10.5194/amt-11-](https://doi.org/10.5194/amt-11-1971-2018)
907 [1971-2018](https://doi.org/10.5194/amt-11-1971-2018)
- 908 Salby, M. L. (1996), *Fundamentals of Atmospheric Physics*. . San Diego, California: Academic
909 Press.
- 910 Sassi, F., Liu, H. L., & Emmert, J. T. (2016), Traveling planetary-scale waves in the lower
911 thermosphere: Effects on neutral density and composition during solar minimum conditions.
912 *Journal of Geophysical Research A: Space Physics*, 121, 1780–1801.
913 <https://doi.org/10.1002/2015JA022082>
- 914 Scherhag, R. (1952), Die explosionsartigen Stratosphärenwärmungen des Spätwinter
915 1951/1952 (The explosive warmings in the stratosphere of the late winter 1951/1952). *Ber.*
916 *Dtsch. Wetterdienstes U.S. Zone*, 38, 51–63.
- 917 Smagorinsky, J. (1953), The dynamical influence of large-scale heat sources and sinks on the
918 quasi-stationary mean motions of the atmosphere. *Quarterly Journal of the Royal*
919 *Meteorological Society*, 79, 342–366.
- 920 Solomon, S., Garcia, R. R., Olivero, J. J., Bevilacqua, R. M., Schwartz, P. R., Clancy, R. T., &
921 Muhleman, D. O. (1985), Photochemistry and Transport of Carbon Monoxide in the Middle
922 Atmosphere. *Journal of Atmospheric Sciences*, 42(10), 1072–1083.
- 923 De Wit, R. J., Hibbins, R. E., Espy, P. J., Orsolini, Y. J., Limpasuvan, V., & Kinnison, D. E.
924 (2014), Observations of gravity wave forcing of the mesopause region during the January

925 2013 major Sudden Stratospheric Warming. *Geophysical Research Letters*, 41, 4745–4752.
926 <https://doi.org/10.1002/2014GL060501>
927